The active CGCG 077-102 NED02 galaxy within the Abell 2063 galaxy cluster

C Adami, K. Parra Ramos, J.T Harry, M.P Ulmer, G.B. Lima Neto, P Amram

A&A 680, A100 (2023)
https://doi.org/10.1051/0004-6361/202244616

Astronomy & Astrophysics

The active CGCG 077-102 NED02 galaxy within the Abell 2063 galaxy cluster⋆

C. Adami[1], K. Parra Ramos[1,3], J. T. Harry[2], M. P. Ulmer[2], G. B. Lima Neto[3], and P. Amram[1]

[1] Aix-Marseille Univ., CNRS, CNES, LAM, 13388 Marseille, France
e-mail: christophe.adami@lam.fr
[2] Department of Physics and Astronomy and CIERA, Northwestern University, 2145 Sheridan Road, Evanston, IL 60208-3112, USA
[3] Instituto de Astronomia, Geofísica e Ciências Atmosféricas, Universidade de São Paulo, Rua do Matão 1226, 05508-090 São Paulo, SP, Brazil

Received 28 July 2022 / Accepted 18 July 2023

ABSTRACT

Context. Within the framework of investigating the link between the central super massive black holes in the cores of galaxies and the galaxies themselves, we detected a variable X-ray source in the center of CGCG 077-102 NED02, which is a member of the CGCG 077-102 galaxy pair within the Abell 2063 cluster of galaxies.
Aims. Our goal is to combine X-ray and optical data to demonstrate that this object harbors an active super massive black hole in its core, and to relate this to the dynamical status of the galaxy pair within the Abell 2063 cluster.
Methods. We used *Chandra* and *XMM-Newton* archival data to derive the X-ray spectral shape and variability. We also obtained optical spectroscopy to detect the expected emission lines that are typically found in active galactic nuclei. Finally, we used public ZTF imaging data to investigate the optical variability.
Results. There is no evidence of multiple X-ray sources or extended components within CGCG 077-102 NED02. Single X-ray spectral models fit the source well. We detect significant, nonrandom inter-observation 0.5–10 keV X-ray flux variabilities, for observations separated by ∼4 days for short-term variations and by up to ∼700 days for long-term variations. Optical spectroscopy points toward a passive galaxy for CGCG 077-102 NED01 and a Seyfert for CGCG 077-102 NED02. The classification of CGCG 077-102 NED02 is also consistent with its X-ray luminosity of over 10^{42} erg s^{-1}. We do not detect short-term variability in the optical ZTF light curves. However, we find a significant long-term stochastic variability in the g-band that can be well described by the damped random walk model with a best-fit characteristic damping timescale of $\tau_{\rm DRW} = 30^{+28}_{-12}$ days. Finally, the CGCG 077-102 galaxy pair is deeply embedded within the Abell 2063 potential, with a long enough history within this massive structure to have been affected by the influence of this cluster for a long time.
Conclusions. Our observations point toward a moderately massive black hole in the center of CGCG 077-102 NED02 of $\sim 10^6\ M_\odot$. As compared to another similar pair in the literature, CGCG 077-102 NED02 is not heavily obscured, perhaps because of the surrounding intracluster medium ram-pressure stripping.

Key words. galaxies: clusters: individual: Abell 2063 – X-rays: galaxies: clusters

1. Introduction

One of the unsolved puzzles of galaxy formation and evolution is the link between the central supermassive black hole (SMBH) in the galaxy core and the galaxy itself: see Latif et al. (2022), Wise et al. (2019), Secrest et al. (2020) and references therein. The existence of a SMBH can give rise to an active galactic nucleus (AGN), with the activity of this latter being enhanced by the fact its galactic host forms a pair; see Pfeifle et al. (2019) for an extensive review of the literature on this topic.

In this framework, a "pair", as defined by Guainazzi et al. (2021), is made of two galaxies separated by less than 150 kpc. Guainazzi et al. (2021) searched for X-ray emission from 32 galaxy pairs that were serendipitously observed by *XMM-Newton* with at least one member classified by the SDSS as an AGN. Using X-ray emission to classify a galaxy as an AGN, these authors found extra AGNs. However, Pfeifle et al. (2019) carried out a similar search and suggested that AGNs in post-merger systems are heavily obscured and that post-mergers can therefore be missed in searches relying on *XMM-Newton* detections. We note that, even though the Pfeifle et al. (2019) search found a pair within one degree of the pair we discuss here (CGCG 077-102 hereafter), their search missed CGCG 077-102, because neither of its members was classified as an AGN in the SDSS database.

Our attention was brought to this pair because, while conducting a search for tidal disruption events (TDEs) in the archival *Chandra* and *XMM-Newton* databases (Maksym et al. 2014, 2013, 2010), we discovered a variable X-ray source. The X-ray source position was within 0.″2 of the nucleus of a galaxy located in the rich cluster of galaxies Abell 2063 ($z = 0.035$, A2063 hereafter). This galaxy is a member of the galaxy pair CGCG 077-102. The two galaxies of this pair (CGCG 077-102 NED01 and CGCG 077-102 NED02, referred to as NED01 and NED02 hereafter) have a very similar appearance in the optical (see Fig. 1) and NED02 is classified as Sab and NED01 as S? in the Siena Galaxy Catalog[1]. In hindsight, the CGCG 077-102 pair could have been found in a search that included both

⋆ Mainly based on observations obtained with *Chandra*, SDSS, and OHP observatories (see acknowledgements for more details).

[1] https://www.legacysurvey.org/sga/sga2020/

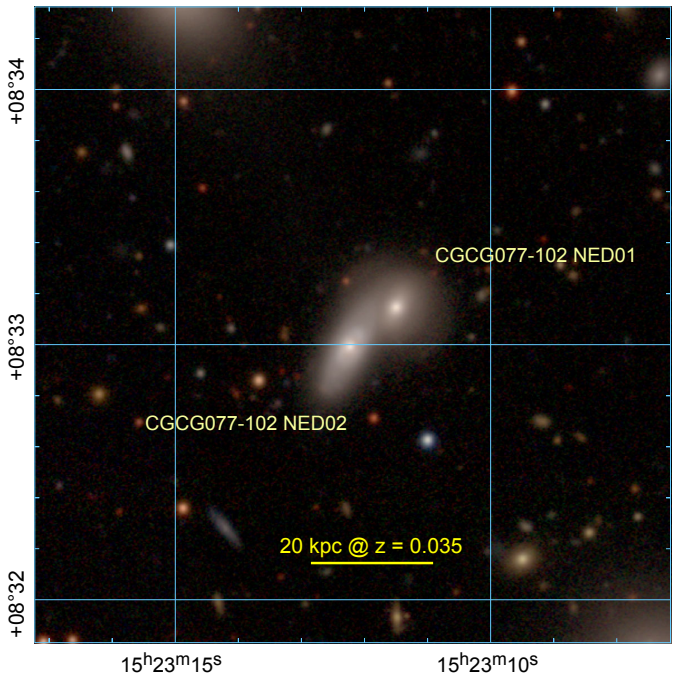

Fig. 1. DESI Legacy *gri* image of the galaxy pair CGCG 077-102. The coordinates are equatorial J2000.0.

a combination of a mid-IR and "hard" (2–10 keV) X-ray detection. In this framework, a search in the WISE database (see Summary and Conclusions) shows that the AGN of the CGCG 077-102 pair (NED02) stands out from the nonAGN by being more than ten times more luminous in the WISE channel 4 (about 22 μ). Therefore, the CGCG 077-102 pair discussed here can be considered a typical example of the kinds of pairs found by Guainazzi et al. (2021), except that the separation in projection is smaller, at only 10 kpc, and the AGN of the pair (see below) was not classified by the SDSS software because no spectrum is recorded in the SDSS database. As the variability did not show a classic $t^{-5/3}$ (e.g., Gezari 2021), we discounted the TDE origin of the X-ray flux from NED02.

The CGCG 077-102 pair is also similar in many ways to the AGN–nonAGN pair J085953.33+131055.3 described in Pfeifle et al. (2019); see their Figs. 2 and 3. Although J085953.33+131055.3 is found in the field as opposed to in an X-ray luminous Abell cluster, both pairs appear to the eye to be spirals, the X-ray-emitting member of the pair is the largest of the two, the redshifts are nearly identical (0.0308 for J085953.33+131055.3 vs. ∼0.035 for CGCG 077-102), and the projected separations are both about 10″ (∼7 kpc). A detailed study of the CGCG 077-102 pair can therefore be used to understand how being in a cluster can affect the accretion flow onto the central SMBH of the AGN member of the pair and the central obscuration.

We were therefore motivated to carry out optical observations in order to determine whether or not it is the X-ray active galaxy of the pair (NED02) that is the only one to exhibit emission lines characteristic of AGN. In the case of CGCG 077-102, as we show in this paper, the X-ray luminosity and the optical emission line spectra are linked.

The outline of this paper is as follows. In Sect. 2, we investigate the X-ray nature of NED02. In Sect. 3, we detail the optical spectroscopy of the CGCG 077-102 pair. Section 4 gives an analysis of the dynamical status of the pair within the A2063 cluster.

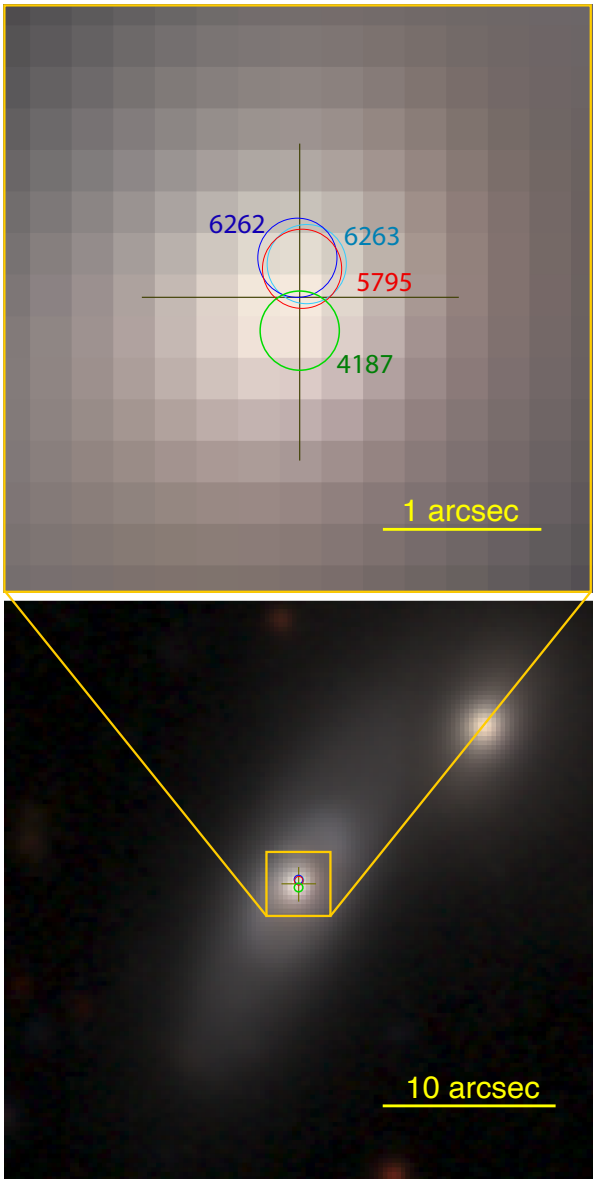

Fig. 2. Center of the X-ray source in each *Chandra* pointing (green, red, blue, and cyan circles of radius 0.25″) superposed on a true-color optical *gri* DESI Legacy Survey image of the galaxy pair CGCG 077-102. Lower panel: NED01/NED02 field. Upper panel: zoom onto NED02. The cross represents the optical center of the galaxy. The pixel size is 0.262″. North is up and east is to the left on both panels.

Section 5 shows the optical light-curve analysis, and in the final section we present our conclusions. Two appendices describe ancillary results.

Throughout the present paper, we use the following cosmological parameters: $H_0 = 69.6\,\mathrm{km\,s^{-1}\,Mpc^{-1}}$, $\Omega_\Lambda = 0.714$ and $\Omega_\mathrm{m} = 0.286$.

2. The X-ray nature of CGCG 077-102 NED02

NED02 has an X-ray source that is present in both the 4XMM-DR11 catalog (Webb et al. 2020) and the *Chandra* Source Catalog 2.0 Evans et al. (2020; see Fig. 2). The *XMM-Newton* catalog contains three measurements and the CSC-2 has four pointings, which we summarize in Table 1.

Table 1. Data from *XMM-Newton* 4XMM-DR11 and *Chandra* CSC-2 catalogs.

4XMM-DR11					CSC-2					
ObsID	Date obs.	exp	off_ax	flux_{XMM}	ObsID	Date obs.	exp	off_ax	Detector	flux_{CSC}
0200120401	2005-02-17	17.4	3.76	2.229	4187	2003-04-20	8.78	4.834	ACIS-I3	0.679
0550360101	2008-07-23	24.4	2.95	1.517	5795	2005-04-02	9.91	5.144	ACIS-S3	1.222
0782531001	2017-01-25	12.0	11.7	2.054	6262	2005-03-28	14.2	5.143	ACIS-S3	1.329
					6263	2005-03-29	16.8	5.143	ACIS-S3	1.393

Notes. The flux is in units of 10^{-12} erg s^{-1} cm^{-2}; for *XMM-Newton*, in the [0.2–12 keV] band, while the *Chandra* flux is in the [0.5–7.0 keV] band. The off-axis distance, off_ax, is in arcmin and the net exposure time, exp, is given in ks.

In both catalogs, the X-ray emission associated with the galaxy NED02 is classified as a point-source. In order to check the automatic pipeline results, we downloaded the publicly available *Chandra* observations and reprocessed the data. We chose to use the *Chandra* data because of the superior spatial resolution, while the total exposure time (adding all observations) is comparable to that of the XMM observation. We therefore combined all four observations listed in Table 1 (the PI was C. Sarazin in all four observations).

The earlier observation from 2003 was carried out with ACIS-I in very faint mode, with the target on the CCD number I3. The other three observations in 2005 were made with ACIS-S – also in very faint mode – using the back-illuminated CCD S3. As the aim-point was the center of Abell 2063, our object of interest, NED02, was always significantly off-center (see Table 1).

For the reprocessing of the downloaded *Chandra* data, we followed the standard procedure described in the CXC Science Threads[2], using CIAO 4.12 and CALDB 4.9.3. We checked for high background periods (flares) in the [0.5–7.0 keV] band by producing light curves with 100 s bins and masking the bright point sources. No such period of flares was found in any of the four exposures.

We then produced a broad-band, exposure-map-corrected image for each exposure (see Fig. 3). The X-ray source in exposure #4187 has a different position angle with respect to the other three pointings; this is why it seems rotated compared to the other images (all images have the same orientation and scale in Fig. 3). We now expand on the potential multiplicity of the X-ray source, as this information is crucial in order to study a potential time-variability.

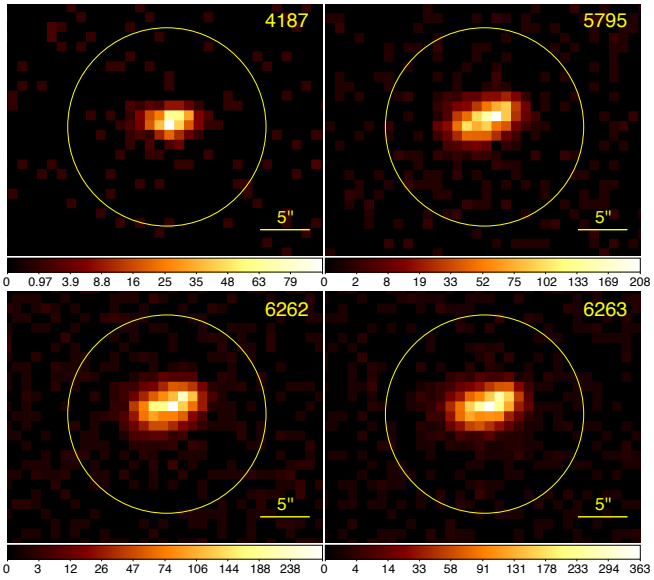

Fig. 3. Exposure-map corrected image of each *Chandra* observations. They are all broad-band, [0.5–7.0 keV]. The color scale is `sqrt` and color bar is in counts per pixel (1 pixel = 0.984″; for this image the "natural" ACIS pixel size was binned by a factor 2). The scale is in counts per pixel. North is up and East is left on all panels.

2.1. Single or multiple X-ray sources within CGCG 077-102 NED02?

We used `ChaRT` v2 to simulate the PSF at the position of the X-ray source and MARX 5.5.1 for creating a simulated event file of a single point source. The point source is modeled using the spectrum of NED02 for each exposure and an observation is simulated using the same characteristics as those of the real observations (offaxis distance, roll-angle, exposure time, very faint mode, and celestial coordinates).

Figure 4 shows an example of a simulated and an observed image corresponding to observation #6263; for the other exposures, the results were very similar. Clearly, the X-ray source can be easily accounted for by a single, spatially unresolved source, affected by the *Chandra* high-resolution mirror assembly (HRMA) telescope point spread function (PSF). There is no evidence of multiple X-ray sources or an extended component. However, an on-axis *Chandra* observation would be the ideal way to use imaging to confirm our supposition that there is a single X-ray source located at the core of NED02.

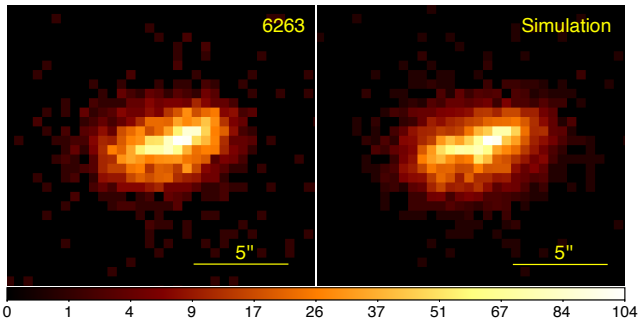

Fig. 4. Image of the *Chandra* observation #6263 (left) compared to the ChaRT+MARX simulation (right). Both images are in the [0.5–7.0 keV] band with a plate scale of 0.492″, the unbinned ACIS pixel size. North is up, East is to the left.

[2] https://cxc.harvard.edu/ciao/threads

Table 2. Results of the single power-law spectral fit for observations #4187, 5795, 6262, and 6263.

Error bars are 90% confidence level								
ObsID	Γ	$N_{\rm H}$ [10^{20} cm^{-2}]	χ^2/d.o.f.	Flux [0.5–7.0 keV]	Flux [0.2–12.0 keV]	Luminosity [0.5–7.0 keV]	Luminosity [0.2–12.0 keV]	cnt
4187	$1.503^{+0.268}_{-0.225}$	$7.807^{+15.008}_{-7.807}$	24.11/28	$0.701^{+0.066}_{-0.087}$	$0.983^{+0.147}_{-0.155}$	$1.96^{+0.18}_{-0.24}$	$2.75^{+0.41}_{-0.43}$	526
5795	$1.748^{+0.137}_{-0.091}$	$0.924^{+3.964}_{-0.924}$	93.07/82	$1.125^{+0.053}_{-0.076}$	$1.510^{+0.105}_{-0.134}$	$3.15^{+0.15}_{-0.21}$	$4.23^{+0.29}_{-0.38}$	1700
6262	$1.679^{+0.027}_{-0.063}$	$0.255^{+2.719}_{-0.255}$	123.28/119	$1.213^{+0.051}_{-0.059}$	$1.651^{+0.097}_{-0.097}$	$3.40^{+0.14}_{-0.17}$	$4.62^{+0.27}_{-0.27}$	2541
6263	$1.875^{+0.095}_{-0.091}$	$2.332^{+2.394}_{-2.246}$	150.15/141	$1.249^{+0.050}_{-0.050}$	$1.635^{+0.091}_{-0.089}$	$3.50^{+0.14}_{-0.14}$	$4.58^{+0.25}_{-0.25}$	3334

Notes. Γ denotes the photon index of the power-law and $N_{\rm H}$ gives the intrinsic hydrogen column density of the source. Fluxes derived from the best fits are in units of 10^{-12} erg s^{-1} cm^{-2}. Luminosities are in 10^{42} erg s^{-1} and "cnt" is the net count (background subtracted).

2.2. X-ray spectral analysis

Next, we checked whether a single absorbed power-law emission could describe the X-ray source. For each exposure, we extracted the spectrum inside a circle of 7″ in radius centered at 15h23m12.21s, +08°32′59.7″ (J2000). The background was also extracted from each exposure within two apertures of 16.4″ in radius centered at 15h23m14.82s, +08°33′19.4″ and 15h23m10.06s, +08°32′35.1″. However, in the case of exposure #4187, accounting for its mismatched position angle, we took a source region of radius 7″ at 15h23m12.23s, +08°32′59.6″ and two background apertures of 16.4″ in radius at 15h23m14.47s, +08°33′21.2″ and 15h23m09.72s, +08°32′37.0″.

For a source with a flux $\sim 10^{-12}$ erg s^{-1} cm^{-2}, some pileup is to be expected. Using the task `pileup_map`, we verified that the level, for the ACIS-I observation #4187, is about 7% on the brightest pixel, dropping to less than 1% four pixels away from the brightest one. For the ACIS-S observations, the brightest pixel has a pileup of around 13%, dropping to 2% four pixels away from the brightest. The relatively low pileup is because the source is far from the *Chandra* "aim point," where the effective area is lower. Therefore, such a minimal pileup may be ignored and did not affect our *Chandra* spectroscopic analysis, nor our interpretation of the results.

For each *Chandra* observation, we computed the rmf and arf files using the CIAO script `specextract`. The spectral fits were done using XSPEC 12.13.0c, with the spectra channels grouped with a minimum of 15 counts per bin, but limited to the range [0.3–7.0 keV]. We used the "Churazov" method for the statistical weight (using the mean value from adjacent energy channels, as recommended in the XSPEC manual), appropriate for small number statistics. The total net count (background subtracted) is shown in Table 2.

We used an absorbed (Galactic and intrinsic) power-law model (xspec `pow`) to fit the observed spectra. The Galactic hydrogen column density was fixed using the HI4PI (HI4PI Collaboration 2016), $N_{\rm H} = 2.61 \times 10^{20}$ cm^{-2}. The resulting best fit is given in Table 2 and shown in Fig. 5. We note that two-component fittings (i.e., fitting with two spectral components, e.g., adding two power-laws) do not give significantly better results and we assume for now that we are dealing with a single component X-ray source.

We note that the best-fit free parameters from the ObsID #4187 are slightly different from the values obtained by fitting the other three exposures (although they are all well within 1σ confidence interval). ObsID #4187 was performed with ACIS-I in faint mode, while the other three were conducted with ACIS-S in very faint mode. Moreover, ObsID #4187 is shallower than the other observations, which explains the larger error bars.

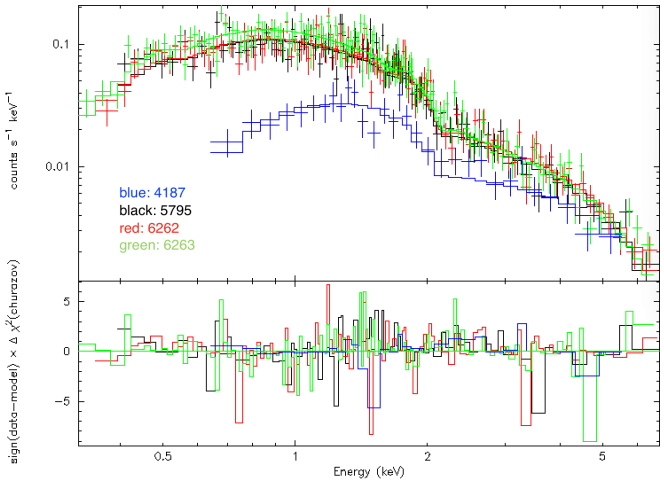

Fig. 5. *Chandra* spectral analysis. *Top*: data with best-fit single power-law model. Each colored line represents a different observation (identified by its ObsID, see Table 1). We note that the ObsID 4187 spectrum (blue curve) was performed with ACIS-I, while the other three were conducted with ACIS-S. *Bottom*: residues (data-model) in terms of the contribution to the χ^2 for each energy bin in the spectrum.

2.3. X-ray variability

We initially made use of the XCTHULHU automated procedure for discovering tidal flare candidates in archival *Chandra* data[3]. Figure 6 shows the X-ray flux from both *Chandra* and *XMM-Newton* observations as a function of time.

To quantify the short-term X-ray variability in each *Chandra* exposure, we implemented the Gregory-Loredo algorithm via CIAO's `glvary` method. An advantage of this implementation is that dither corrections for an exposure are applied by re-normalizing the light curve, which means the variability is not flagged by any dither modulation across the ACIS chips. In assigning a single variability index (in the range from 0 to 10) to an observation, the algorithm conditions over: the probability that the source flux is not constant over the observation exposure time; the combinatoric "total odds ratio" from binning N events into M time bins; and the fractions of the light curve within 3σ and 5σ, respectively, of the average count rate in a given exposure. An index ≥6 signifies that a given light curve is "definitely variable", corresponding to high probability of nonconstant flux ($P \sim 1$) and/or high total odds ratio $O \gtrapprox 2$. The $3\sigma/5\sigma$ light-curve fractions are only relevant at low variability index.

For NED02, ObsIDs 4187, 6262, and 6263 were flagged as definitely not variable with index 0. However, ObsID 5795 was

[3] https://github.com/xcthulhu/Galaxy-Clusters

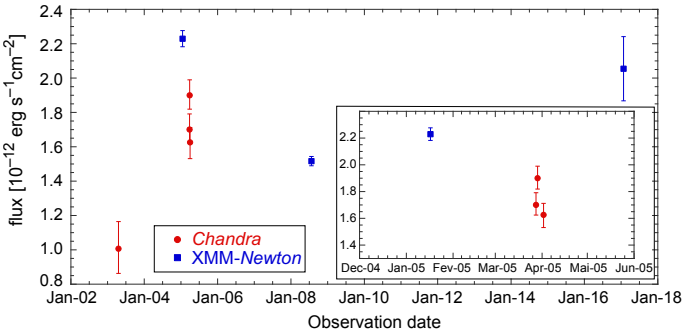

Fig. 6. X-ray flux [0.2–12.0 keV] extrapolated from the fitted spectrum for *Chandra* data and from the archive for *XMM-Newton* data, as a function of time. The inset at the bottom right is a zoom onto the period from December 2005 to June 2005.

flagged as definitely variable with index 7, which is attributable to a non-negligible decrease in flux over its exposure time. As a control, we tested the variability of the diffuse emission within the background apertures for the ObsID 6263 exposure, which `glvary` flagged as nonvariable with index 0.

To assess the X-ray variability of NED02 in greater detail, we consider (1) the long-term variability across all four exposures and (2) the long-term variability across the most recent three exposures (omitting ObsID 4187). For each case, the X-ray light curve was grouped into 500 s bins, and bins with zero count rate were discarded to consider only nontrivial X-ray detections in the variability analysis. To quantify the variability of this light curve, we implemented the long-term variability measures described in De Luca et al. (2021). The results are shown in Table 3.

We therefore conclude that we have a significant inter-observation X-ray variability that is likely nonrandom. We now investigate the variable nature of NED02 in the optical wavelengths.

3. Optical spectroscopy of the CGCG 077-102 galaxy pair

NED01 galaxy member of the CGCG 077-102 pair is a $z \sim 0.03439$ passive galaxy (star formation rate approximately equal to zero from SDSS DR17 database: see StarformingPort model[4] for more details) observed by the SDSS survey (obj. id: 1937715310949853184). Its population age is estimated to 9.75 (between 8.5 and 10.75) Gyr (PassivePort model).

NED02, the other pair member, is at $z \sim 0.03662$ (e.g., Lee et al. 2017). To the best of our knowledge, there is no publicly available optical spectrum for this object, even in the SDSS database. In order to deeply investigate the spectral characteristics of the CGCG 077-102 pair, we mapped it at the Observatoire de Haute-Provence with two instruments.

3.1. MISTRAL observations

MISTRAL is a low-resolution single-slit spectro-imager[5]. We used it in February 2022 to observe the CGCG 077-102 pair. We selected the blue setting (1 h exposure, $R \sim 750$, covered wavelength range: [4200, 8000]A) to observe two different slits (see Fig. 7). The MISTRAL slit aperture is fixed to 1.9″. Spectra were wavelength-calibrated using a combination of Hg, Ar, and Xe lamps. Wavelength calibration exposures were taken just after the science exposures, before making any significant telescope and instrument move. Flux calibration was based on the simultaneous observation of the HD 289002 spectrophotometric standard.

Data reduction was performed with the MISTRAL dedicated night spectral Python-based data reduction tool. This code is based on the Automated SpectroPhotometric Image REDuction package (Lam et al. 2022, ASPIRED[6]) and has been tuned to the MISTRAL needs.

The first observed slit was placed to cover the central area of the two galaxies. The second one was to sample the northern outskirts of the pair. We obtained good enough signal-to-noise to extract spectra in six different regions (see Fig. 7 and Table 4).

First, region #4, covering the center of NED01 (1.9″ × 11″), shows a MISTRAL spectrum that is very similar to the SDSS spectrum (see Fig. 7) when rescaled to take into account the different apertures (SDSS is a 3″ circle, different from the MISTRAL extraction area). No emission lines are visible, and we detect deep absorption lines (Hβ, MgI, CaFe, NaD, and perhaps even Hα). Region #6 does not show any emission lines. Absorption lines, such as Hβ, MgI, and NaD, are visible. We therefore confirm the passive status of NED01. None of the explored regions in this galaxy show any sign of gas ionization.

The situation is clearly different for NED02. The external area (region #5: 1.9″ × 11″) does not show any emission lines. We may detect MgI and Ca/Fe. The three other regions (#1, 2, 3: 1.9″ × 2.4″) exhibit clear [OIII], Hα, and [SII] emissions. More remarkably, regions #1 and 3 exhibit prominent [NII]@6585A emissions, as strong as the Hα line itself. We detect absorption MgI, Ca/Fe, and NaD lines in regions #1 and #3. We also note that Hβ is not present, that is, in either emission or absorption, in regions #1, #2, or #3. It is therefore clear that emission lines are only present close to the NED02 center (see below for high-resolution integral field GHASP spectroscopic observations as well). We note that region #1 includes the X-ray source detected in *Chandra* data.

These emission lines coming preferentially from the NED02 center are possibly due to an AGN in the galaxy center. However, with the galaxy pair probably interacting, we may have some merging-induced star formation in NED02. To check this hypothesis, we first used the AMAZED spectral fitting code (e.g., Schmitt et al. 2019). Among the 21 available in the code, the template offering the best fit is a quasi stellar object (QSO) with a metalicity of 0.5 and a stellar population age of 5 Gyr.

We then measured the fluxes under the lines (see Table 5) using the SLINEFIT (e.g., Schreiber et al. 2018) public code[7]

[4] The StarformingPort and PassivePort models from the SDSS database estimate the stellar masses of SDSS and BOSS galaxies with the Portsmouth method and star-forming and passive models. Stellar masses come from the method of Maraston et al. (2009). These fit stellar evolution models to the SDSS photometry, using the known spectroscopic redshifts and assuming the Kroupa initial mass function Kroupa (2001). For the star-forming case, the star-formation model uses a metallicity and one of three star-formation histories: constant, truncated, and exponentially declining. For passive models, the model is an instantaneous burst stellar population whose age is fit for (with a minimum allowed age of 3 Gyr). The population is 97% solar metallicity and 3% metal-poor, by mass. We refer the reader to `https://skyserver.sdss.org/dr18/MoreTools/browser`

[5] `http://www.obs-hp.fr/guide/mistral/MISTRAL_spectrograph_camera.shtml`

[6] `https://github.com/cylammarco/ASPIRED`

[7] `https://github.com/cschreib/slinefit/blob/master/README.md`

Table 3. Variability measures for the long-term NED02 X-ray light curves for the *Chandra* exposures, quantifying the variability size and timing.

	χ^2_ν/p-value [a]	MDDE [b]	MR/MRE [c]	TMDDE [d]	WMEAN [e]	EMFU/EMFD [f]	TEMFU/TEMFD [g]
All four ObsIDs	15.662/	9.129	11.400/	708.51	0.132	5.588/	709.49/
	~0		14.021			2.033	4.24
4187 omitted	2.420/	5.515	2.553/	4.24	0.183	1.766/	0.79/
	5.327×10^{-12}		0.070			2.033	4.24
			ET2U/ET2D [h]	ET10U/ET10D [i]	Z_{WW} [j]		
		All 4 ObsIDs	708.49/	n.a./	−10.768		
			4.24	n.a.			
		4187 Omitted	n.a/	n.a./	−12.658		
			4.24	n.a			

Notes. [a]Reduced $\chi^2 = \frac{1}{n-1}\sum_i^n \left(\frac{x_i-\bar{x}}{\sigma_i}\right)^2$ about the error-weighted mean count rate, and the corresponding p-value. p-values <0.0027 are deemed significant (i.e., nonvariability is improbable) at a 3σ level. [b]Maximum error-normalized count rate change, in counts per second. [c]Ratio of maximum count rate to the minimum count rate (MR) and the propagated error (MRE). [d]Time interval for the largest error-normalized count rate change, in days. [e]Error-weighted mean count rate, in counts per second. [f]Maximum upward/downward count rate ratio $\left(\frac{x_i-\sigma_i}{x_j+\sigma_j}\right)_{\max}$ for $i > j$ (EMFU), $i < j$ (EMFD). [g]Corresponding time intervals for EMFU and EMFD, in days. [h]Shortest time interval (in days) for a count rate increase (ET2U) or decrease (ET2D) by a factor >2, i.e., where $\frac{x_i-\sigma_i}{x_j+\sigma_j} > 2$. If no such interval exists, we report as n.a. [i]Shortest time interval (in days) for a count rate increase (ET10U) or decrease (ET10D) by a factor >10, i.e., where $\frac{x_i-\sigma_i}{x_j+\sigma_j} > 10$. [j]$Z$ test statistic for the Wald-Wolfowitz runs test. At 5% significance ($|Z| < 1.96$), one should accept a null hypothesis of random variability.

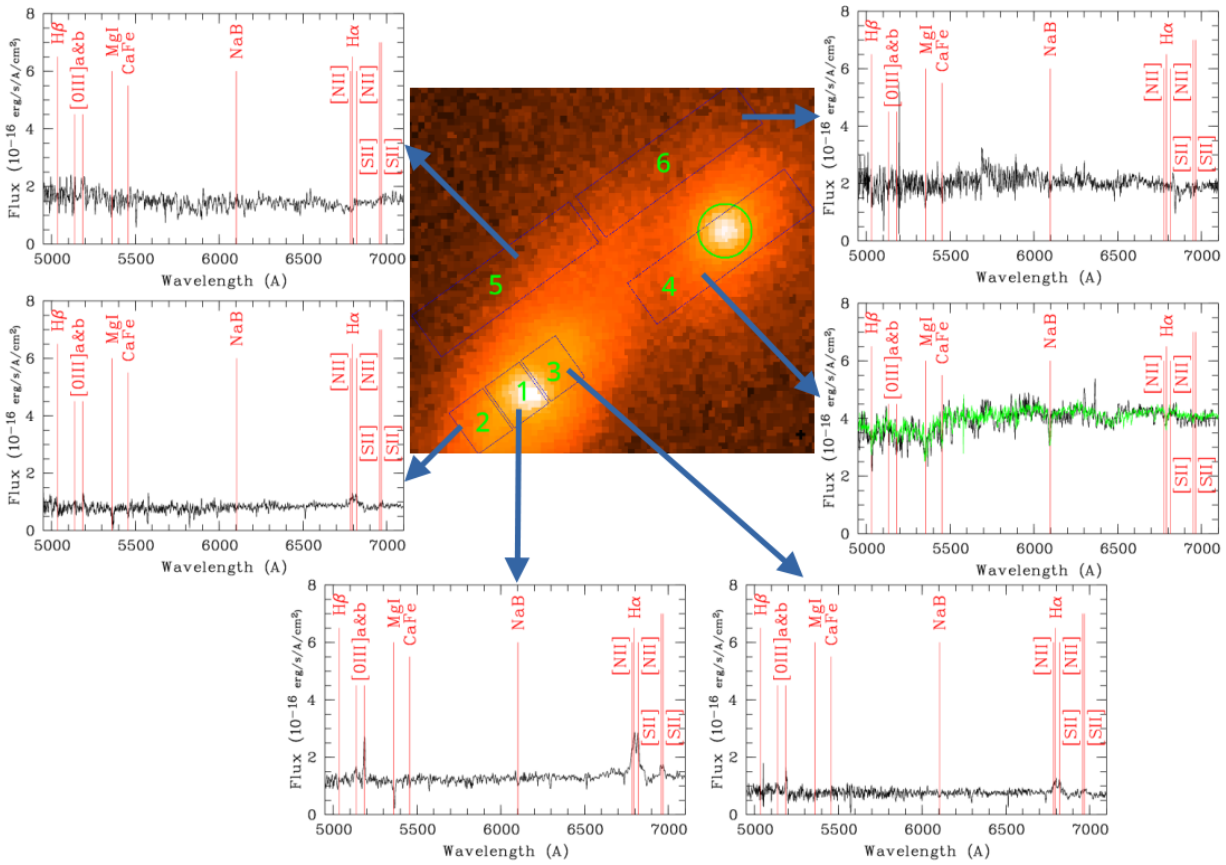

Fig. 7. MISTRAL spectroscopic observations of six different regions of CGCG 077-102. Spectra are flux calibrated. The location of the SDSS fiber is shown as the green circle. The SDSS spectrum (green spectrum) is superimposed over the MISTRAL spectrum (black spectrum) for region #4.

to generate line ratios. We used the Hα/NII@6584A and O[III]@5007A/Hβ lines ratio in order to place NED02 (region #1) in the Fig. 8 diagram. With Hβ being undetected, we instead used the 3σ noise within the [5000;5100]A range in order to generate a lower limit for O[III]@5007A/Hβ. Figure 8 also shows the Kauffmann et al. (2003) and Kewley et al. (2013) separations between normal galaxies and active objects.

We see that the NED02 region #1 has optical AGN characteristics. From Richardson et al. (2014: see their Fig. 1), Márquez et al. (2017: see their Fig. 1), and Kehrig et al. (2012),

Table 4. Integrated and surface brightness magnitudes of the six spectroscopically sampled regions (see Fig. 7).

Region id	g' integrated [mag]	g' surface brightness [mag arcsec^{-2}]	Size [arcsec]
1	17.4	19.5	1.9×2.4
2	18.6	20.7	1.9×2.4
3	18.1	20.2	1.9×2.4
4	17.0	20.7	1.9×11
5	18.9	22.6	1.9×11
6	18.7	22.4	1.9×11

Notes. We also give the angular size of the regions. Magnitudes are computed from the public SDSS g'-band images of the region.

Table 5. Hβ, [OIII]@5007, Hα, and [NII]@6584 fluxes measured in region #1, in units of erg s^{-1} cm^{-2}.

Hβ	[OIII]@5007	Hα	[NII]@6584
$\leq 3. \times 7.7 \times 10^{-17}$	1.5×10^{-15}	4.1×10^{-15}	5.0×10^{-15}

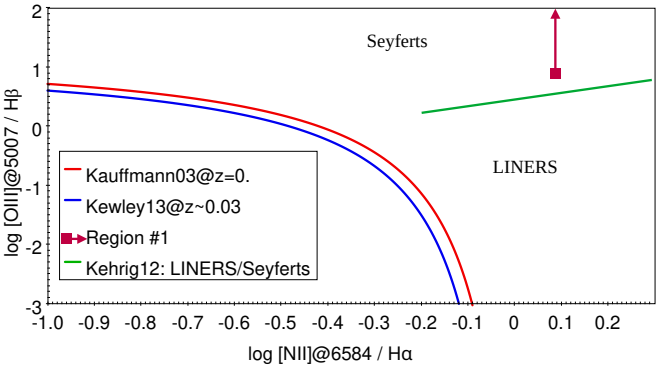

Fig. 8. log([OIII]5007/Hβ) vs. log([NII]6584A/Hα) for MISTRAL region #1 spectrum. From Kauffmann et al. (2003) and Kewley et al. (2013), the areas under the red and blue curves are for normal galaxies, while areas above these curves are for active objects. The green line shows the delimitation between Seyfert and LINERS galaxies (Kehrig et al. 2012). The vertical dark magenta arrow is to indicate that NED02 Region 1 has detectable Hα, N[II]6584 and O[III]5007 emissions but no detectable Hβ flux. The bottom of this line shows the minimal value from the lower detection limit of Hβ.

we classify NED02 as a generic Seyfert based on the line flux ratios in the spectrum. To add further weight to the Seyfert classification, we can note that the X-ray luminosity of NED02 is between 10^{42} and 10^{43} erg s^{-1}. This places the NED02 X-ray luminosity in the range of other local Seyferts (e.g., Márquez et al. 2017). The power-law spectral indices and Nh values are also typical of AGNs (see e.g., Vasylenko et al. 2015). From a qualitative point of view, the optical spectrum of NED02 is also very different from type I AGNs. It exhibits narrow emission lines, contrary to type I AGN detected in Abell 2163 by Maurogordato et al. (2008: see their Fig. 1) for example.

These optical spectroscopic data, despite covering a large wavelength domain and allowing the detection of several spectral lines, are nevertheless limited by their low resolution: $R \sim 750$. They are therefore not adapted to computing velocity dispersions. Moreover, they do not cover 100% of the galaxy area. In order to bypass these limitations, we obtained integral field spectroscopic data for a very small spectral domain. These are strategically selected around the Hα/[NII] emission lines, and are described in the following subsection.

3.2. GHASP observations

High-resolution Integral Field Unit (IFU) spectroscopy was obtained with the Fabry-Perot instrument GHASP used on the OHP 193 cm telescope on 20 March 2023 with a ~3 arcsec seeing. GHASP has a field of view of 5.8×5.8 arcmin^2, and is coupled with a 512×512 Image Photon Counting System (IPCS) with a pixel size of 0.68×0.68 arcsec^2. It has a spectral resolution that depends on the Fabry-Perot interferometer chosen; here $R \sim 11\,000$, see Gach et al. (2002). The full spectral range of 492 km s^{-1} of the Fabry-Perot at the redshifted wavelength of the galaxy was scanned through 48 channels. The data reduction procedure adopted to reduce the GHASP data is extensively described in Epinat et al. (2008) and Gómez-López et al. (2019).

The central velocity dispersion of the gas of NED02 was estimated from GHASP data (Fig. 9) to be 11.2 ± 1 km s^{-1} (tentatively corrected for the spectral resolution of the instrument and based on the Hα line), or 15.5 ± 1 km s^{-1} uncorrected. The velocity dispersion was measured considering that the Hα emission can be modeled by a Gaussian function in dividing the measured

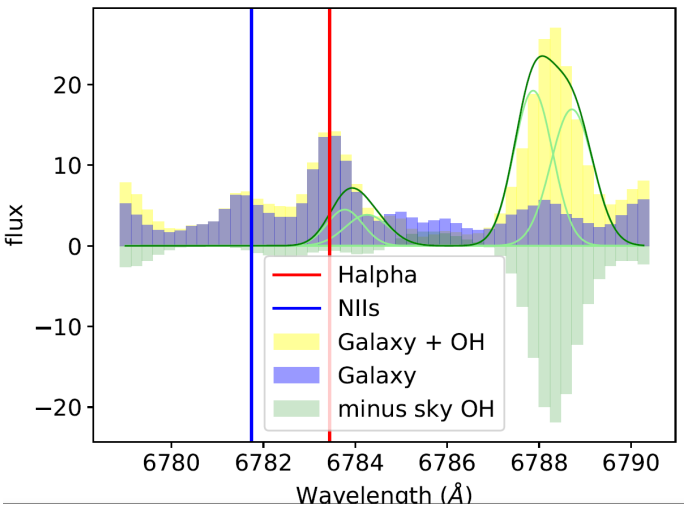

Fig. 9. GHASP high-resolution spectrum of the Hα/[NII] region measured on an area of ~4.6 arcsec^2 centered on the nucleus of the galaxy. Flux is in arbitrary units. The light green Gaussian curves are the expected individual OH night sky emission lines convolved at the line spread function of the instrument (~10.7 km s^{-1}). The dark green curve is the sum of the light green lines. The mirrored light green histogram is the galaxy-free OH night sky lines measured on a region of ~3.2 arcmin^2 around the galaxy. The net galaxy emission is given by the purple histogram. Vertical blue and red lines are the expected redshifted location of the [NII]@6584 and Hα, respectively. Due to the cyclic nature of the Fabry-Perot interferometer, the redshifted [NII]@6584 is shifted by minus two free spectral ranges (one FSR ~ 11.51 Å) to the blue and is thus observed at ~−2 Å from the Hα line.

FWHM by $2\sqrt{2\ln 2}$. The measure was made within an area of ~4.6″^{2}, which is equivalent to ~2.2 kpc^2 at the redshift of the galaxy pair.

We used Oh et al. (2022) to statistically translate this value into a stellar velocity dispersion estimate of 34 ± 1 km s^{-1} (corrected) and 41 ± 1 km s^{-1} (not corrected). This can be directly related to the mass of the central black hole. Tremaine et al. (2002) gave $M_{\rm BH} = 1.2 \times 10^5\ M_\odot$ (corrected) and $M_{\rm BH} = 2.6 \times 10^5\ M_\odot$ (uncorrected). Given the uncertainties in the relations of

Oh et al. (2022) and Tremaine et al. (2002), and our own uncertainty on the central velocity dispersion of the gas, the upper value of the mass is $M_{\rm BH} = 5.3 \times 10^5\,M_\odot$. This value corresponds to the lower limit we estimate in Sect. 5.4 based on the optical variability of the core of NED02 (see below).

Finally, no significant Hα emission was detected outside of the NED02 core. Some signal may be present to the northern outskirts of the galaxy, north of MISTRAL extraction region #5, but the noise is too high to make this potential detection significant.

4. Dynamical status of the CGCG 077-102 pair in A2063

We now investigate the dynamical status of the pair CGCG 077-102 in A2063 in order to detect possible effects of the large-scale structure in the NED02 AGN behavior. The spatial distribution of galaxies within the A2063 field of view (with available spectroscopic redshifts in NED) is shown in Fig. 10. This catalog includes 177 galaxies with spectroscopic redshifts.

CGCG 077-102 was selected to be included in a 1deg radius from the cluster center. This represents a physical ~2.5 Mpc radius. A2063 has a measured X-ray temperature of ~4.1 keV Ebeling et al. (1998). This translates into a total mass of $4 \times 10^{-14}\,E(z)\,M_{500}\,h_{70}^{-1}$ Lieu et al. (2016), which is equivalent to a radius of ~1.5 Mpc. Our catalog therefore covers the whole of the densest part of the cluster.

In order to also select the densest cluster parts along the redshift axes, we chose to select the redshift range where the velocity gap between two consecutive galaxies along the line of sight is larger than 200 km s^{-1} (Adami et al. 1998, for a similar technique). This leads to a cut in the redshift range between $z = 0.0285$ and $z = 0.03963$, which corresponds to approximately ±2.6 cluster velocity dispersions (estimated to be 639 km s^{-1}, see below).

We searched for substructures by appling the Serna–Gerbal method (Serna & Gerbal 1996, SG hereafter) to the velocity catalog. This hierarchical method allows cluster substructures to be extracted from a catalog containing positions, magnitudes, and velocities based on the calculation of their relative negative binding energies. The method produces a list of galaxies that belong to the selected substructures, as well as information on their binding energy. We used a M/L ratio in the V-band of 100. We checked that using M/L ratios between 100 and 400 does not induce the detection (or the absence of detection) of additional cluster substructures.

The SG method reveals the existence of a main bulk (the most tightly bound galaxies inside the cluster potential well, assumed to constitute the cluster seed). The galaxies in this bulk have a typical extension on the sky of ~50 kpc (see Fig. 10) and their velocity dispersion is 317 km s^{-1}. When considering all the galaxies in the cluster, the velocity dispersion is 639 km s^{-1}. In addition, eight galaxy dynamical pairs are also detected. Their positions are displayed in Fig. 10. The most tightly bound pair in terms of cluster potential is the pair studied in the present paper (CGCG 077-102: NED01 and NED02). Less than 5% of the known cluster galaxy members are more deeply embedded in the cluster potential wheel (see Fig. 11). Moreover, Fig. 10 shows that the CGCG 077-102 pair is very centrally located inside the cluster, which is contrary to all other pairs, which are detected inside the cluster outskirts.

This clearly means that the CGCG 077-102 pair is not a recent member of A2063 and has had enough time to fall deep inside the cluster potential. The pair has been under the influence of the cluster for a long time.

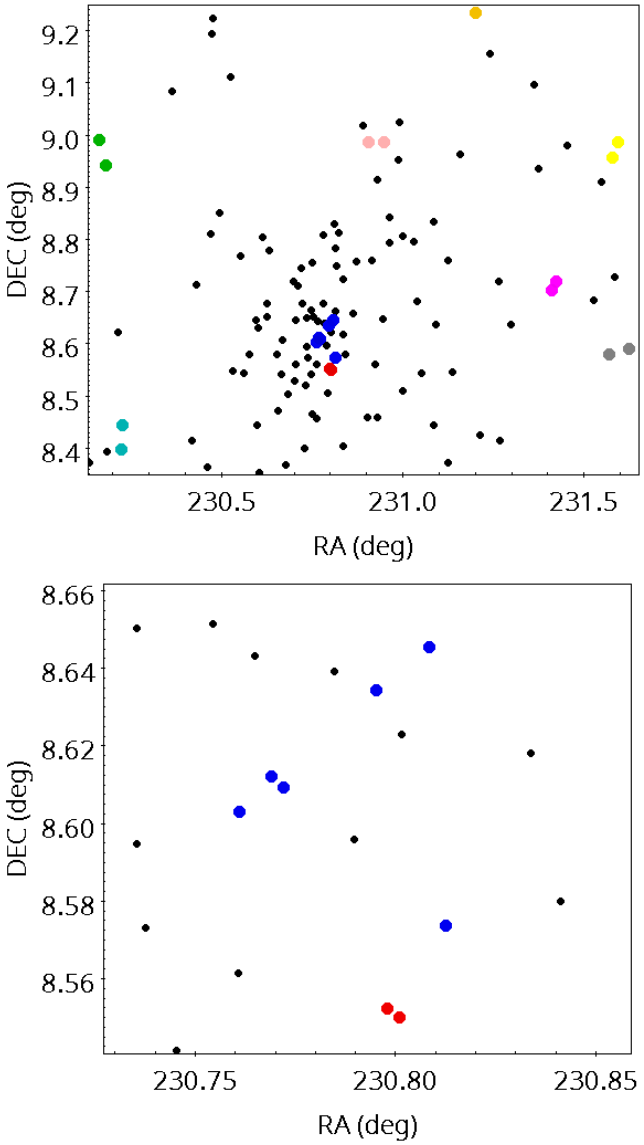

Fig. 10. Sky distribution (within the A2063 field of view) of the galaxies with a measured spectroscopic redshift (from NED) between 0.0285 and 0.03963 (black dots). The cluster bulk (as determined by the SG method) is shown as blue filled circles. The CGCG 077-102 pair is shown by the red filled circles. Other SG-detected pairs are shown with the other filled circles with different colors. Top: full field of view. Bottom: zoom onto the cluster center.

Our MISTRAL optical follow-up was not regular enough to allow a study of the flux variability of the NED02 core. We therefore used the Zwicky Transient Facility (ZTF) for this purpose, which we describe in the following section.

5. Optical light-curve analysis of CGCG 077-102 NED02

In many works, the flux or magnitude variability is often used to complement the systematic identification of AGNs in samples with a large amount of data, such as multi-epoch surveys e.g., Trevese et al. (2008), Young et al. (2012), De Cicco et al. (2015), Poulain et al. (2020), or Burke et al. (2022). The variability is an important characteristic observed in all wavelength ranges of the electromagnetic emission of AGNs because it can be related to physical processes that occur in their accretion disk

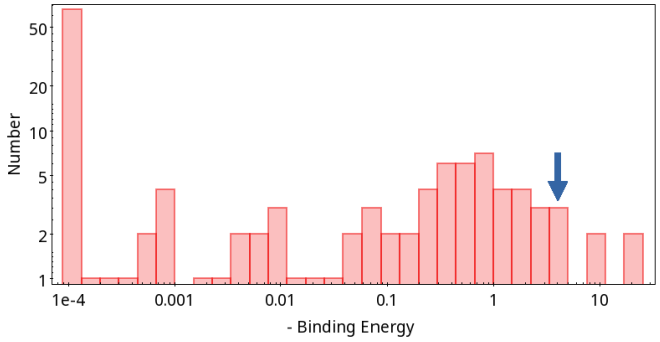

Fig. 11. Binding energy histogram obtained by applying the SG technique for the 177 galaxies shown in Fig. 10. The x-axis is the relative binding energy (in arbitrary units). The y-axis shows the number of galaxies for a given binding energy. The CGCG 077-102 pair is shown as the vertical arrow.

and jets (see Padovani et al. 2017). However, the mechanisms responsible for this variability still need to be better understood. In this section, we describe the datasets and the time-series optical analysis of the galaxy NED02. We aim to quantify the optical variability associated with the AGN activity as well as to search for a periodic (or quasi-periodic) behavior in the light curves to understand the mechanisms behind the interactions of the galaxy pair.

5.1. Zwicky Transient Facility DR15

We used public data made available in the 15th data release of the Zwicky Transient Facility (ZTF), a time-domain survey that uses the 1.22 m Samuel Oschin Schmidt telescope at the Palomar Observatory and a 47 deg^2 field-of-view camera to cover the northern sky in r, g, and i optical filters (Bellm et al. 2019; Graham et al. 2019), in order to obtain four years of observations from NED02 and its companion NED01. All details about the data-processing pipeline (ZTF Science Data System, ZSDS) are described in Masci et al. (2019).

We selected the nearest sources inside 5″ from the optical center of the galaxies on ZTF, which correspond to light curves in r, i, and g filters. As the data from each filter and CCD quadrant are processed separately by the ZTF pipeline, we found multiple light curves in the same filter for a single object. However, the combination of these multiple light curves can introduce spurious variability due to the calibration differences (van Roestel et al. 2021). For this reason, we chose to study the light curves with the highest number of observations. Also, because of the small number of observations, we excluded the i band light curve from our analysis (see Table 6 for details).

In addition, we obtained all light curves through the ZTF application program interface[8], where we applied a filter in a search parameter (`BAD_CATFLAGS_MASK=32768`) to select the observation epochs with high image quality flags (i.e., `catflags=0`). This criterium excludes observation epochs affected by clouds and/or the moon, as described in the ZTF documentation[9].

5.2. Noise removal

We noticed some similarities between the light curves of NED02 and those of other galaxies in the neighborhood of the A2063 cluster by visual inspection, suggesting the existence of an unknown source of noise affecting extended objects at this observed field in the same epochs.

The presence of systematic and random trends in light curves may be associated with atmospheric events (such as cloud passages and air masses), instrumental effects (CCD noise and telescope vibration), and imperfections in the data reduction (e.g., flat fielding). This can introduce false positives, leading us to misinterpret the results (e.g., false detection of periodic or quasi-periodic signals in AGNs). Several works have also reported similar problems in the light curves of their targets (e.g., Pont et al. 2006; Kim et al. 2010; Mislis et al. 2010; Gibson et al. 2013).

Several methods and tools to improve the signal-to-noise ratio of the light curves are available in the literature, such as detrending algorithms (e.g., Kovács et al. 2005; Tamuz et al. 2005; or Kim et al. 2009), smoother filters (e.g., Savitzky & Golay 1964), and Bayesian methods (e.g., Taaki et al. 2020). In this work, we used the Photometric DeTrending Algorithm Using Machine Learning[10] (PDT, Kim et al. 2009), which applies a balanced iterative reduction and clustering using a hierarchical algorithm (BIRCH, Zhang et al. 1996) in its latest version to identify common trends in a set of light curves used as templates. After that, the algorithm constructs master trends that are then used to remove trends from individual light curves (see Kim et al. 2009 for more details).

We must consider some aspects before selecting a set of light curves used as templates by PDT.

- The light curves must be synchronized in time.
- We have to select a template set of bright objects that are not saturated.
- It is recommended to choose nonvariable objects (or at least a high number of them) in the same field as the target, because the algorithm is sensitive to the choice of light curves (Kim et al. 2009).
- The PDT manual recommends having a template set of at least 50 light curves to run the code.

However, the sample selection process becomes challenging, because there are not enough objects that follow these requirements in the same field as NED02 and that have data available on ZTF in all filters used. Therefore, we instead selected the galaxy companion NED01, which is a passive galaxy, as described in Sect. 3. By definition, the galaxy pair was observed in the same epochs, in the same weather conditions, and was susceptible to the same instrumental errors. Also, due to the passive state of NED01, we do not expect variability in its light curve related to physical processes on the SMBH. Therefore, we assumed it could be used as a light curve reference to subtract the noise in the galaxy NED02 because the PDT detects similarities between light curves.

We ran the code using a template set composed of NED01 and NED02 light curves to find master trends. After that, we detrended the NED02 light curve. The error propagation was computed using a Monte Carlo method (see BIPM, Iec, IFCC 2008)[11], as described below:

[8] https://irsa.ipac.caltech.edu/docs/program_interface/ztf_lightcurve_api.html
[9] https://irsa.ipac.caltech.edu/data/ZTF/docs/releases/ztf_release_notes_latest
[10] https://github.com/dwkim78/pdtrend
[11] https://www.bipm.org/en/committees/jc/jcgm/publications

Table 6. Four nearest sources from the optical center of NED02 and NED01.

Galaxy	oid [(a)]	Filter	Nobs [(b)]	Selected
CGCG 077-102 NED02	531302400031665	*i*	91	No
	531202400030069	*r*	422	Yes
	1526110300008580	*g*	11	No
	531102400013043	*g*	300	Yes
CGCG 077-102 NED01	531102400008167	*g*	300	Yes
	531202400023741	*r*	422	Yes
	1526110300018677	*g*	11	No
	531302400029994	*i*	91	No

Notes. [(a)]The object identifier of ZTF. [(b)]Number of public observations with high image quality flag.

1. We added noise to the original data to simulate a sample of 50 new light curves.

$$m = m_0 + \sigma_0 \cdot \sigma_{\rm noise}, \tag{1}$$

where m is the detrended magnitude, m_0 is the magnitude of the nondetrended light curve, σ_0 is the uncertainty of m_0, and $\sigma_{\rm noise}$ is the random noise generated from a normal distribution of mean 0 and variance 1.
2. After detrending each simulated light curve with the same master trends computed before by the PDT, we calculated the standard deviation of each observation epoch to get the new uncertainty.
3. Due to a significant spread in the magnitudes measured in the same night, the final step in our time series analysis was calculating the mean of intranight observations. The light curves before and after the noise correction are shown in Fig. 12.

Finally, we repeated the last three steps (detrending, error propagation, and mean of the intranight observations) for the NED01 light curves only for comparison. The results are shown in Appendix A.

5.3. Optical variability

5.3.1. Excess variance

The normalized excess variance, $\sigma^2_{\rm NXS}$, introduced by Nandra et al. (1997), measures the intrinsic variability of an object due to the existence of measurement errors that will contribute to an "extra variance" in the data (Vaughan et al. 2003). In this work, we used the unnormalized version of the excess variance in magnitude units to quantify the variability of the light curves, which is defined as

$$\sigma^2_{\rm XS} = S^2 - \left\langle \sigma^2_{\rm err} \right\rangle, \tag{2}$$

where S^2 is the variance of the light curve and $\left\langle \sigma^2_{\rm err} \right\rangle$ is the mean square error:

$$\left\langle \sigma^2_{\rm err} \right\rangle = \frac{1}{N_{\rm obs}} \sum_{i=1}^{N_{\rm obs}} \sigma^2_{{\rm err},i}, \tag{3}$$

where $N_{\rm obs}$ is the number of observations and $\sigma_{{\rm err},i}$ is the uncertainty of the individual magnitude i. Following Yuk et al. (2022), the error in the excess variance is

$$\Delta(\sigma^2_{\rm XS}) = \sqrt{\frac{2}{N_{\rm obs} - 1}} S^2. \tag{4}$$

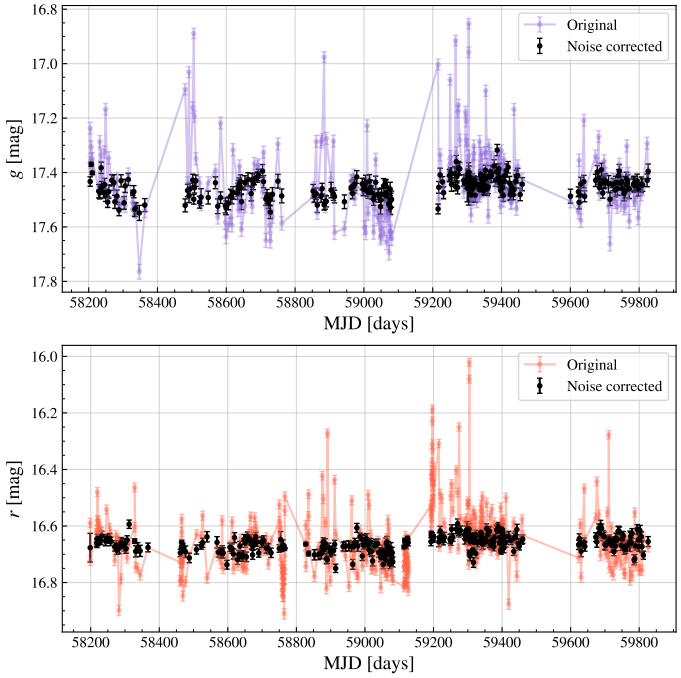

Fig. 12. Comparison between the light curves in g (top panel) and r (bottom panel) bands of NED02 before and after the noise correction with PDT and calculation of the intranight observation mean. The purple and orange connected dots represent the original light curves in their respective filters (g and r), and the black dots with error bars represent the noise-corrected light curve.

The excess variance is often used as a selection parameter to determine whether or not the object has sufficient variability to be considered as an AGN of a certain class (e.g., Yuk et al. 2022; López-Navas et al. 2023). In addition, several authors have studied its correlation with physical properties, such as the $\sigma^2_{\rm NXS}$–$M_{\rm BH}$ correlation in X-ray data (e.g., Ponti et al. 2012; Zhou et al. 2010), which means that estimations of this parameter could potentially be very useful (see Padovani et al. 2017).

5.3.2. Variability results

The histograms of magnitude distribution before and after noise correction are shown in Fig. 13. First, we observed that the magnitude distribution of the light curve became more compact around the mean value after the noise correction, that is, the observed variability decreased. On the other hand, the magnitudes are widely spread before the correction, and their

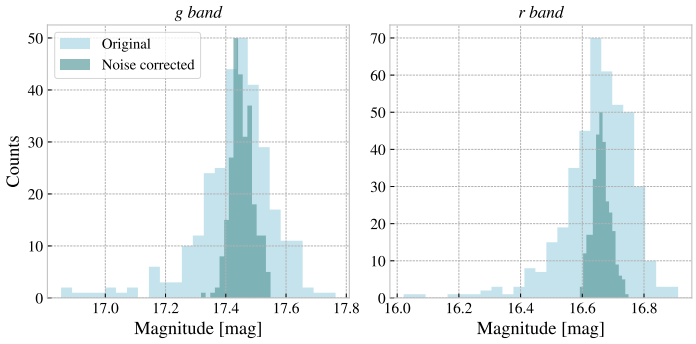

Fig. 13. Histograms of magnitude distribution before (light blue) and after (dark turquoise) the noise correction of NED02 light curves in g (left) and r (right) bands.

distribution is asymmetric, showing a tail on the left side in the direction of low magnitudes (negative value for skewness, see Table 7). However, this is likely a consequence of the presence of outliers, and we can confirm this with more observations to check whether or not the pattern repeats itself. The statistical results of the NED02 light curve are given in Table 7.

We noticed a difference in the mean level value of the first three and last two cycles[12] of the light curve observations in both filters (see Table 7). This behavior is present even before the detrending process of the light curves and seems to happen in both filters quasi-simultaneously (Fig. 12), indicating that it cannot be an artifact introduced by the PDT code. Thus, new observation cycles will help us understand the nature of this very long-timescale variability pattern. If the very long-term variability (from years to decades) is genuine, then a small excess variance (or normalized excess variance) is expected because this latter is more sensitive to short-term variability, and most of the observing magnitudes are around the light curve mean until now.

We do not detect a short-term variability on timescales from weeks to months in any filter (Table 7). We expected a nearly constant profile for the NED01 light curve, but it appears to have some artifacts (see Appendix A), and therefore we cannot exclude the possibility of a signal amplitude over-subtraction during the detrending process. Despite the small excess variance (before and after the noise correction), this variance is still more significant in the g-band than in the r-band. The variability on timescales from months to years in the detrended light curves is also more significant in the g-band (see Fig. 12). Regarding the long-term variability, a detailed discussion is described in Sect. 5.4. Furthermore, several studies have detected larger variability amplitudes on timescales from months to years in optical bands than in the X-rays, while on timescales from hours to days, the variability observed in the X-rays is larger than in the optical: Arévalo et al. (2008, 2009), Uttley et al. (2003), and references therein. In general, the challenging task of distinguishing the lower luminosity AGNs from the normal galaxies in the optical wavelengths is evident due to the observed low optical variability (see also Padovani et al. 2017). Therefore, the optical variability as a unique criterium for AGN selection might be insufficient.

In the future, we will improve the techniques for noise removal to avoid biases and misinterpretation of the results through our requested optical telescope time to perform intra-night observations, which will help us identify outliers, better estimate the noise, and confirm whether or not NED02 has a very short variability (on timescales from hours to a few days).

[12] We define a cycle of observations as an interval of quasi-sequential data surrounded by a long period without observations. For example, the light curves used were obtained over five cycles of observations.

5.4. Periodicity: Damped random walk

In this section, we describe one of two methods used to model and characterize the long-term oscillatory behavior observed in the g-band light curve of NED02. We did not analyze the r-band in order to avoid the incorrect estimation of constraints because of its low variability (Sect. 5.3.2) and the nonexistence of possible periodic trends that can be distinguished from the likely unknown artifacts introduced during the detrending process without any bias, as shown in Figs. 12 and A.2. A detailed description of the second method, the Lomb-Scargle periodogram analysis, can be found in Appendix B.

The damped random walk (DRW) is a stochastic model often used to describe the accretion-disk variability of AGNs (Kelly et al. 2009). It is the lowest-order model of the continuous-time autoregressive moving average (CARMA) models introduced by Kelly et al. (2014; see Moreno et al. 2019, for a review). The DRW model gives a PSD characterized by a white noise slope ($\propto f^0$) at low frequencies and a red noise slope ($\propto f^{-2}$) at high frequencies, where the transition between these regions indicates a frequency related to a characteristic damping timescale, $\tau_{\rm DRW} = (2\pi f_{\rm DRW})^{-1}$, that is correlated with black hole mass (Kelly et al. 2009; Burke et al. 2021).

In this work, we use the `Celerite` (Foreman-Mackey et al. 2017) Python package to implement the Gaussian process (GP) regression and to build the DRW kernel function with an additional white-noise term (also called jitter term) to model the NED02 light curve. Then, we use the `emcee` (Foreman-Mackey et al. 2013) package to implement the Markov chain Monte Carlo (MCMC) sampler algorithm to analyze the posterior probability distribution, assuming uniform priors for all free parameters. For all parameters, we computed the median of the MCMC samples and their 16th and 84th percentiles for the uncertainties. The covariance function (kernel) of the DRW with an additional jitter term is given by

$$k(t_{nm}) = 2\sigma^2_{\rm DRW} \exp(-t_{nm}/\tau_{\rm DRW}) + \sigma^2_{\rm WN}\delta_{nm}, \quad (5)$$

where $\sigma_{\rm DRW}$ is the amplitude term, $t_{nm} = |t_n - t_m|$ is the time lag between the measurements t_m and t_n, $\sigma_{\rm WN}$ is the amplitude of the white-noise signal, and δ_{nm} is the Kronecker delta function.

The best-fitting DRW model that describes the entire detrended light curve of NED02 (Fig. 14) gives the parameters $\tau_{\rm DRW} = 30^{+28}_{-12}$ days, $\sigma_{\rm DRW} = 0.18^{+0.01}_{-0.01}$ mag, and $\sigma_{\rm WN} = 0.009^{+0.005}_{-0.009}$ mag. The posterior probability distributions of the fitted parameters are shown in Fig. 15, and the power spectrum density of the DRW model is shown in Fig. 16.

We computed the supermassive black hole mass constraints using the $\tau_{\rm DRW}-M_{\rm BH}$ scale relations available in the literature in order to compare it with the one we obtained from the velocity dispersion measures of the optical spectra. Following Kelly et al. (2009), we find $M_{\rm BH} = 10^{6.73^{+0.51}_{-0.39}}\,M_\odot$. From Burke et al. (2021), we have $M_{\rm BH} = 10^{6.65^{+0.72}_{-0.55}}\,M_\odot$, and $M_{\rm BH} = 10^{6.43^{+0.91}_{-0.70}}\,M_\odot$ for the Wang et al. (2023) relation. The transitional frequency, $f_{\rm DRW} = 0.0053^{+0.0034}_{-0.0025}$ days^{-1}, is not compatible with the $f_{\rm break}$ computed in the Lomb-Scargle analysis (Appendix B). This is an expected result because we analyzed only a small region of the light curve in the Lomb-Scargle periodogram analysis. Also, the Lomb-Scargle method expects to model periodic signals, which is probably not the case for NED02.

Table 7. Statistical values of the NED02 light curves before and after noise correction in both filters (g and r).

	ZTF g-band		ZTF r-band	
Parameter	Original light curve	Noise corrected	Original light curve	Noise corrected
$m_{\rm mean}$ [(a)]	17.43 ± 0.01	17.454 ± 0.002	16.65 ± 0.01	16.662 ± 0.002
$\sigma^2_{\rm XS}$	0.017 ± 0.001	0.0009 ± 0.0001	0.013 ± 0.001	0.0006± 0.0001
$m_{\rm max}$ [(b)]	17.76	17.55	16.91	16.75
$m_{\rm min}$ [(c)]	16.85	17.32	16.02	16.59
$m_{(1-3)}$ [(d)]	17.46 ± 0.01	17.473 ± 0.003	16.69 ± 0.01	16.677 ± 0.002
$m_{(4-5)}$ [(d)]	17.41 ± 0.01	17.437 ± 0.003	16.60 ± 0.01	16.647 ± 0.002
Skewness	−1.3	0.04	−1.4	0.25

Notes. The parameters ($m_{\rm mean}$, $\sigma^2_{\rm XS}$, $m_{\rm max}$, and $m_{\rm min}$) are in units of magnitude. [(a)]Mean value of the light curve. [(b)]Maximum magnitude. [(c)]Minimum magnitude. [(d)]Mean level of the observed cycles interval of the light curve in units of magnitude.

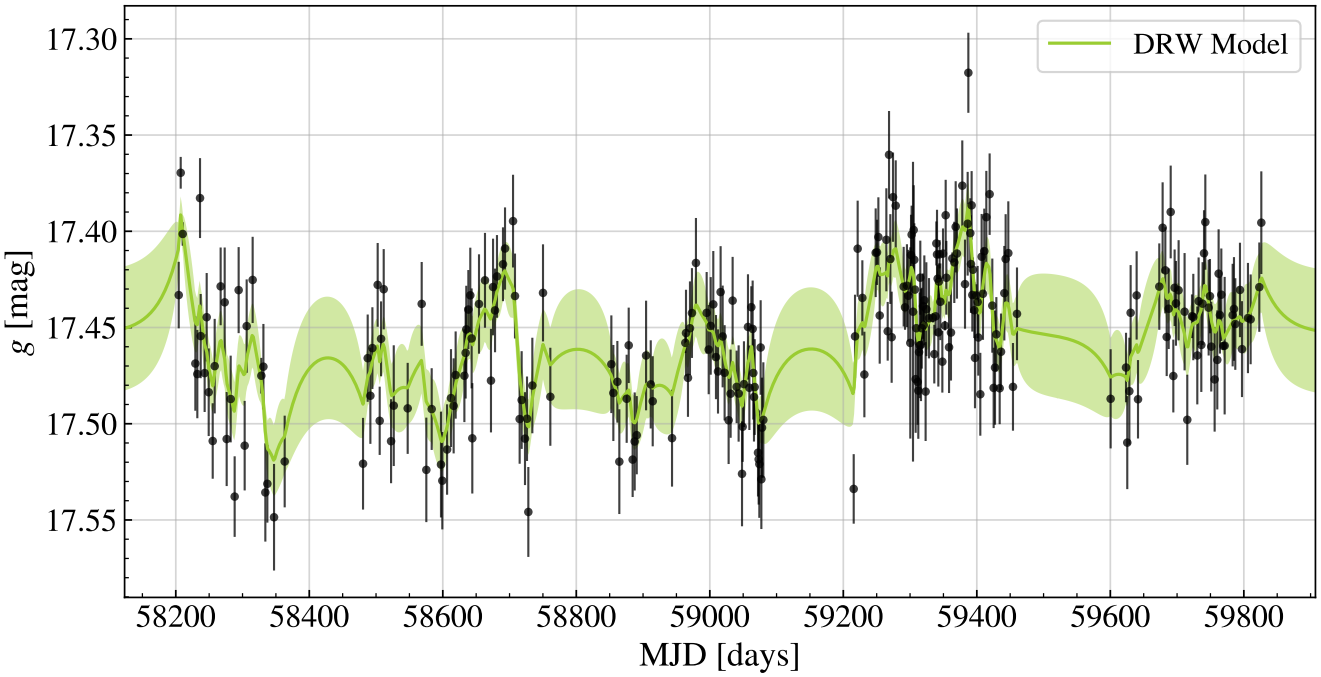

Fig. 14. Detrended light curve of NED02 in g-band (black dots). The best-fitting DRW model with a 1σ of uncertainty (shaded area) is shown in green. The 1σ uncertainty is the 16th and 84th percentiles of the MCMC sample.

Stochastic models usually give a good description of the well-sampled continuous AGN light curves. However, the DRW model can deviate from the real light curves in the presence of gappy data or limited length, introducing bias on the predicted parameters (Kozłowski 2017). Furthermore, recent studies have shown that some AGN light curves require more flexible models (e.g., Mushotzky et al. 2011; Zu et al. 2013; Kasliwal et al. 2015; Guo et al. 2017), such as high-order CARMA models (Kelly et al. 2014) that do not have a fixed PSD as in the DRW (Moreno et al. 2019). For example, the variability driven by multiple processes in the accretion disk or other unknown perturbations can be responsible for deviations from the DRW model (Zu et al. 2013; Dobrotka et al. 2017; Guo et al. 2017; Moreno et al. 2019).

Here, we show that NED02 has an optical light curve better described by the DRW model than by our classical mass method, as in the other AGNs found in the literature. This means that NED02 has aperiodic stochastic variability over long timescales. However, we must be careful with the estimated parameters given all the potential issues related to the detrending process mentioned above, degeneracy in DRW modeling (Kozłowski 2016), and the possible bias introduced in the $\tau_{\rm DRW}-M_{\rm BH}$ relations found in the literature, which is due to the restricted samples of these studies (Burke et al. 2021).

In future work, we will take advantage of our submitted proposals to obtain quasi-simultaneous optical and X-ray observations with MISTRAL and *Chandra* telescope. This will allow us to study the existence of time delays in the optical emission regarding the X-rays, as well as to compare their variability amplitudes on different timescales, which can shed some light on the scenarios that try to explain the physical processes responsible for the optical emission of the accretion disk. Moreover, more observation cycles will be available in the next ZTF data releases, meaning an increase in the NED02 light-curve length. Consequently, we will be able to improve the accuracy of the parameter fitting with the DRW model. Also, we will verify whether more flexible high-order CARMA models are necessary to model the light curve given the possibly

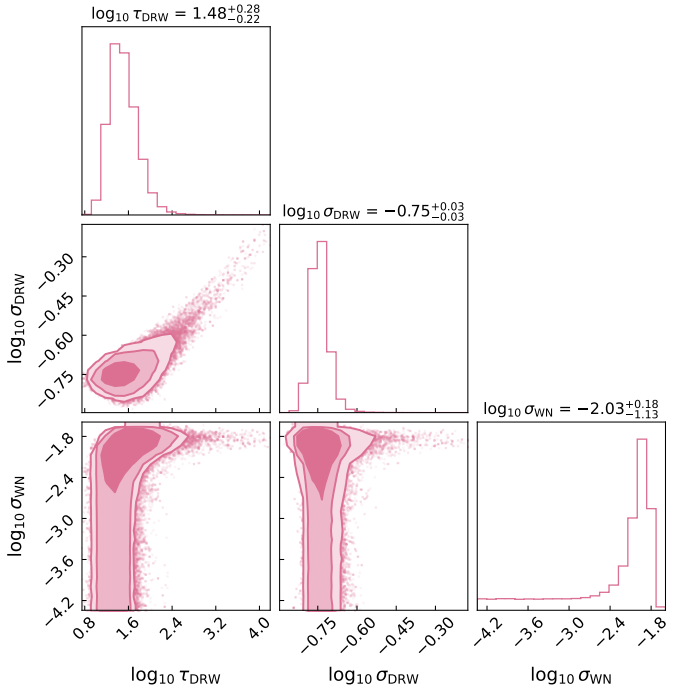

Fig. 15. Posterior probability distributions of the parameters from the DRW and jitter kernels. The contours show 68%, 95%, and 99% confidence intervals, and the pink dots are the MCMC samples. The parameter $\tau_{\rm DRW}$ is in units of days, and the amplitudes ($\sigma_{\rm DRW}$ and $\sigma_{\rm WN}$) are in units of magnitude. The parameter uncertainties were computed using the 16th and 84th percentiles of the MCMC samples.

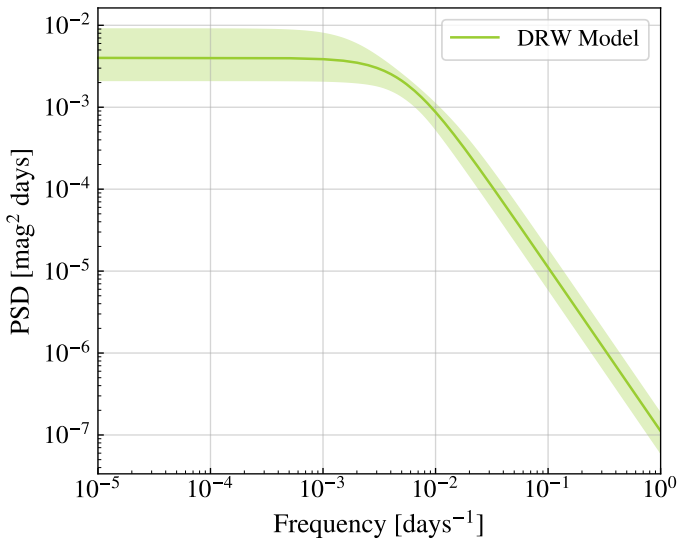

Fig. 16. Power spectrum density of the best-fitted DRW model obtained with `Celerite` (solid green line). The green shaded area shows the region between the 16th and 84th percentiles. The characteristic frequency that defines the transition between the white and red noise in the PSD is $f_{\rm DRW} = 0.0053^{+0.0034}_{-0.0025}$ days^{-1}.

more complex processes that are only evident on very long timescales.

6. Summary and conclusions

In the framework of investigating the link between central super massive black holes in the core of galaxies and the galaxies themselves, we detected a variable X-ray source in the CGCG 077-102 galaxy pair. In Table 8, we display typical magnitudes of NED01 and NED02 drawn from the WISE catalog[13]. Only one of the members of the pair harbors an AGN, namely NED02. This latter also stands out as being the only one present in the list in longer wavelengths in the *Spitzer* source catalog; for example, in the MIP 70 µm band and in the X-rays (see Table 2). Therefore, literature searches for galaxy pairs with at least one AGN did not find the NED01–NED02 pair.

Using *Chandra* data and the *XMM-Newton* catalog, we showed that there is no evidence of multiple components or of an extended component within the X-ray source. Only new on-axis *Chandra* data would allow us to definitively confirm whether or not there is a single X-ray source in the core of NED02. However, single X-ray spectral models do not produce poorer fittings than two-component models, and the X-ray source is within 0.2″ of the core. Therefore, the X-ray emission is most likely coming from a single X-ray source associated with a SMBH. We therefore considered but rejected a model with two X-ray sources; first, because a two-component model was not needed to fit the X-ray spectrum, and second because the position of the X-ray source is within the error of the optical nucleus of the galaxy.

We find that the 0.5–10 keV flux varies between observations by factors of up to ∼2 and this variation is likely nonrandom. We show a short-term X-ray variability over a timescale of ∼4 days and a long-term variability over a timescale of ∼700 days. However, we reject the possibility that we detected a TDE because no typical decay $t^{-5/3}$ was observed, nor the typical black body spectrum with kT near 0.1 keV (e.g., Gezari 2021).

To characterize this source at optical wavelengths, we also obtained low-resolution optical spectroscopy in order to detect characteristic spectral lines over extended areas of the galaxy pair. NED01 only shows absorption lines, regardless of the position tested in the galaxy. We are therefore dealing with a passive object. NED02 only shows strong emission lines in the galaxy center. This shows that no significant induced star formation (potentially due to gravitational interactions between NED01 and NED02) is present in the galaxy outskirts. The central emission lines are most probably due to a central active object, probably a Seyfert.

We also obtained high-resolution optical spectroscopy covering a short wavelength range around the Hα/[NII] domain. We then derived a robust central velocity dispersion that we translate into a central black hole mass of a few $10^5\,M_\odot$. This estimate is smaller than, but not inconsistent with, the one we derived using the optical variability. Given our uncertainties, we therefore conclude that the central black hole has a mass of the order of $\sim 10^6\,M_\odot$.

We detect no short-term variability in the optical ZTF light curves. However, we find a significant long-term stochastic variability in the g-band that can be well described by the damped random walk model with a best-fit characteristic damping timescale of $\tau_{\rm DRW} = 30^{+28}_{-12}$ days.

Finally, we show that the CGCG 077-102 galaxy pair is deeply embedded within the Abell 2063 cluster potential. Only 5% of the cluster galaxies are more closely linked with the cluster potential than the CGCG 077-102 pair.

[13] This publication makes use of data products from the Wide-field Infrared Survey Explorer, which is a joint project of the University of California, Los Angeles, and the Jet Propulsion Laboratory/California Institute of Technology and is funded by the National Aeronautics and Space Administration.

Table 8. Summary of IR fluxes for NED02 and NED01.

ID	WISE	J	H	K_s	WISE4
NED01	J152311.51+083308.7	14.832	14.216	13.944	9.087
NED02	J152312.25+083259.1	14.695	13.980	13.530	6.534

As noted in Sect. 1, CGCG 077-102 is comparable to the J085953.33+131055.3 pair discussed in Pfeifle et al. (2019). However, unlike the J085953.33+131055.3 system, the X-ray source of CGCG 077-102 is not heavily absorbed. Pfeifle et al. (2019) hypothesized that the proximity of a neighboring galaxy produced enhanced accretion on the X-ray emitting nucleus of the other galaxy. Enhanced accretion in their model then led to enhanced column densities of $N_{\rm H}$ of order $10^{23}\,{\rm cm}^{-2}$. The X-ray source in the nucleus of NED02 has a much lower best fit to its $N_{\rm H}$, that is, of the order of $10^{20}\,{\rm cm}^{-2}$. With the caveat that only the projected separation of J085953.33+131055.3 and CGCG 077-102 are similar, an explanation of the lower value of Nh for the CGCG 077-102 system is that ram pressure stripping by the ICM of A2063 has removed (or has partially removed) the source of Nh, which would otherwise have been available to produce a high value of $N_{\rm H}$ obscuration. The detection of more such CGCG 077-102 pairs in rich clusters will help us to decipher whether or not ram pressure stripping was the cause of the lower value of $N_{\rm H}$ of the X-ray-emitting AGN of the CGCG 077-102 pair.

Our black hole mass estimates are based on an analysis of the optical spectrum and optical flux variation of the central region of NED02, which suggest values of a few times $10^5\,M_\odot$ and a few times $10^6\,M_\odot$, respectively. Yet another method would be to take the Eddington limit for spherical accretion (e.g., Rybicki & Lightman 1979; Greene et al. 2020) with an X-ray luminosity of the black hole of about $1.3\times10^{38}\,{\rm erg\,s}^{-1}$, and then to use a value of $5\times10^{42}\,{\rm erg\,s}^{-1}$ (based on the typical X-ray luminosity we derived; see Table 2) for the X-ray luminosity to infer a lower bound on the mass of the central SMBH, giving a lower limit of about $4\times10^4\,M_\odot$. The lower end of our mass estimates puts the mass at the top of the intermediate black hole (IMBH) mass range (Greene et al. 2020). Therefore, we may have found an IMBH. However, the mass estimate based on the optical spectrum lies just above the value of $10^5\,M_\odot$ at the low end of the $M\sigma$ extrapolation discussed by Greene et al. (2020), who state that they are confident that central SMBHs extend to $10^5\,M_\odot$. Furthermore, Greene et al. (2020) suggest the highest time variability is expected to come from the most compact emitting region, namely the X-ray-emitting region. Therefore, searching for random and quasi-periodic oscillations (QPOs) will be an interesting follow-up project. Evidence for QPOs in the X-rays and its relationship to the mass of the central SMBH has been discussed, for example, by Smith et al. (2021), Agarwal et al. (2021), and Secrest et al. (2020). Based on the results of these latter authors, and the mass we estimate for the SMBH in NED02, a plausible range of frequencies we could hope to detect in X-ray observations is approximately 10^{-3}–10^{-4} Hz. These are low enough to justify a search within further observations with satellites such as *XMM-Newton* and NICER.

Acknowledgements. Authors thank the referee for useful comments. Authors thank F. Durret, P. Theulé, V. LeBrun, and I. Marquez for useful discussions. Authors thank J. Schmitt for his great contribution to the MISTRAL building and maintenance. Funding for the Sloan Digital Sky Survey IV has been provided by the Alfred P. Sloan Foundation, the U.S. Department of Energy Office of Science, and the Participating Institutions. SDSS-IV acknowledges support and resources from the Center for High-Performance Computing at the University of Utah. The SDSS web site is www.sdss.org. SDSS-IV is managed by the Astrophysical Research Consortium for the Participating Institutions of the SDSS Collaboration including the Brazilian Participation Group, the Carnegie Institution for Science, Carnegie Mellon University, the Chilean Participation Group, the French Participation Group, Harvard-Smithsonian Center for Astrophysics, Instituto de Astrofísica de Canarias, The Johns Hopkins University, Kavli Institute for the Physics and Mathematics of the Universe (IPMU)/University of Tokyo, the Korean Participation Group, Lawrence Berkeley National Laboratory, Leibniz Institut für Astrophysik Potsdam (AIP), Max-Planck-Institut für Astronomie (MPIA Heidelberg), Max-Planck-Institut für Astrophysik (MPA Garching), Max-Planck-Institut für Extraterrestrische Physik (MPE), National Astronomical Observatories of China, New Mexico State University, New York University, University of Notre Dame, Observatário Nacional/MCTI, The Ohio State University, Pennsylvania State University, Shanghai Astronomical Observatory, United Kingdom Participation Group, Universidad Nacional Autónoma de México, University of Arizona, University of Colorado Boulder, University of Oxford, University of Portsmouth, University of Utah, University of Virginia, University of Washington, University of Wisconsin, Vanderbilt University, and Yale University. The DESI Legacy Imaging Surveys consist of three individual and complementary projects: the Dark Energy Camera Legacy Survey (DECaLS), the Beijing-Arizona Sky Survey (BASS), and the Mayall z-band Legacy Survey (MzLS). DECaLS, BASS and MzLS together include data obtained, respectively, at the Blanco telescope, Cerro Tololo Inter-American Observatory, NSF's NOIRLab; the Bok telescope, Steward Observatory, University of Arizona; and the Mayall telescope, Kitt Peak National Observatory, NOIRLab. NOIRLab is operated by the Association of Universities for Research in Astronomy (AURA) under a cooperative agreement with the National Science Foundation. Pipeline processing and analyses of the data were supported by NOIRLab and the Lawrence Berkeley National Laboratory (LBNL). Legacy Surveys also uses data products from the Near-Earth Object Wide-field Infrared Survey Explorer (NEOWISE), a project of the Jet Propulsion Laboratory/California Institute of Technology, funded by the National Aeronautics and Space Administration. Legacy Surveys was supported by: the Director, Office of Science, Office of High Energy Physics of the U.S. Department of Energy; the National Energy Research Scientific Computing Center, a DOE Office of Science User Facility; the U.S. National Science Foundation, Division of Astronomical Sciences; the National Astronomical Observatories of China, the Chinese Academy of Sciences and the Chinese National Natural Science Foundation. LBNL is managed by the Regents of the University of California under contract to the U.S. Department of Energy. The Siena Galaxy Atlas was made possible by funding support from the U.S. Department of Energy, Office of Science, Office of High Energy Physics under Award Number DE-SC0020086 and from the National Science Foundation under grant AST-1616414. Based in part on observations made at Observatoire de Haute Provence (CNRS), France, with GHASP and MISTRAL. This research has made use of the MISTRAL database, operated at CeSAM (LAM), Marseille, France. K.P.R. acknowledges financial support of the Coordenação de Aperfeiçoamento de Pessoal de Nível Superior (CAPES), Grant No. 88887.694541/2022-00. GBLN acknowledges partial financial support from CNPq grant 303130/2019-9. Software Used: SLINEFIT (Schreiber et al. 2018), ASPIRED (Lam et al. 2022), numpy (Harris et al. 2020), astropy (Astropy Collaboration 2022), scipy (Virtanen et al. 2020), matplotlib (Hunter 2007), corner (Foreman-Mackey 2016), emcee (Foreman-Mackey et al. 2013), celerite (Foreman-Mackey et al. 2017). Authors thank the CNES for financial support of the MISTRAL operations.

References

Adami, C., Biviano, A., & Mazure, A. 1998, A&A, 331, 439
Agarwal, A., Rani, P., Prince, R., et al. 2021, Galaxies, 9, 20
Arévalo, P., Uttley, P., Kaspi, S., et al. 2008, MNRAS, 389, 1479
Arévalo, P., Uttley, P., Lira, P., et al. 2009, MNRAS, 397, 2004
Astropy Collaboration (Robitaille, T. P., et al.) 2013, A&A, 558, A33
Astropy Collaboration (Price-Whelan, A. M., et al.) 2018, AJ, 156, 123
Astropy Collaboration (Price-Whelan, A. M., et al.) 2022, ApJ, 935, 167
Bellm, E. C., Kulkarni, S. R., Graham, M. J., et al. 2019, PASP, 131, 018002P

BIPM, Iec, IFCC, et al. 2008, Evaluation of measurement data - Supplement 1 to the "Guide to the Expression of Uncertainty in Measurement" - Propagation of Distributions using a Monte Carlo Method, Joint Committee for Guides in Metrology, JCGM 101:2008
Burke, C. J., Shen, Y., Blaes, O., et al. 2021, Science, 373, 789
Burke, C. J., Liu, X., Shen, Y., et al. 2022, MNRAS, 516, 2736
De Cicco, D., Paolillo, M., Covone, G., et al. 2015, A&A, 574, A112
De Luca, A., Salvaterra, R., Belfiore, A., et al. 2021, A&A, 650, A167
Dobrotka, A., Antonuccio-Delogu, V., & Bajčičáková, I. 2017, MNRAS, 470, 2439
Ebeling, H., Edge, A. C., Bohringer, H., et al. 1998, MNRAS, 301, 881
Epinat, B., Amram, P., & Marcelin, M. 2008, MNRAS, 390, 466
Evans, I. N., Primini, F. A., Miller, J. B., et al. 2020, Am. Astron. Soc. Meet. Abstr., 235, 154.05
Foreman-Mackey, D. 2016, J. Open Source Softw., 1, 24
Foreman-Mackey, D., Hogg, D. W., Lang, D., & Goodman, J. 2013, PASP, 125, 306
Foreman-Mackey, D., Agol, E., Ambikasaran, S., & Angus, R. 2017, AJ, 154, 220
Gach, J. L., Hernandez, O., Boulesteix, J., et al. 2002, PASP, 114, 1043
Gezari, S. 2021, ARA&A, 59, 21
Gibson, N. P., Aigrain, S., Barstow, J. K., et al. 2013, MNRAS, 428, 3680
Gómez-López, J. A., Amram, P., Epinat, B., et al. 2019, A&A, 631, A71
Graham, M. J., Kulkarni, S. R., Bellm, E. C., et al. 2019, PASP, 131, 078001
Greene, J. E., Strader, J., & Ho, L. C. 2020, ARA&A, 58, 257
Guainazzi, M., De Rosa, A., Bianchi, S., et al. 2021, MNRAS, 504, 393
Guo, H., Wang, J., Cai, Z., & Sun, M. 2017, ApJ, 847, 132
Harris, C. R., Millman, K. J., van der Walt, S. J., et al. 2020, Nature, 585, 357
HI4PI Collaboration (Ben Bekhti, N., et al.) 2016, A&A, 594, A116
Hunter, J. D. 2007, Comput. Sci. Eng., 9, 90
Kasliwal, V. P., Vogeley, M. S., & Richards, G. T. 2015, MNRAS, 451, 4328
Kauffmann, G., Heckman, T. M., Tremonti, C., et al. 2003, MNRAS, 346, 1055
Kehrig, C., Monreal-Ibero, A., Papaderos, P., et al. 2012, A&A, 540, A11
Kelly, B. C., Bechtold, J., & Siemiginowska, A. 2009, ApJ, 698, 895
Kelly, B. C., Becker, A. C., Sobolewska, M., Siemiginowska, A., & Uttley, P. 2014, ApJ, 788, 33
Kewley, L. J., Dopita, M. A., Leitherer, C., et al. 2013, ApJ, 774, 100
Kim, D.-W., Protopapas, P., Alcock, C., Byun, Y.-I., & Bianco, F. B. 2009, MNRAS, 397, 558
Kim, D. W., Protopapas, P., Alcock, C., et al. 2010, AJ, 139, 757
Kovács, G., Bakos, G., & Noyes, R. W. 2005, MNRAS, 356, 557
Kozłowski, S. 2016, MNRAS, 459, 2787
Kozłowski, S. 2017, A&A, 597, A128
Kroupa, P. 2001, MNRAS, 322, 231
Lam, M. C., Lam, M. C., Smith, R. J., et al. 2022, ASP Conf. Ser., 532, 537
Latif, M. A., Whalen, D. J., Khochfar, S., Herrington, N. P., & Woods, T. E. 2022, Nature, 607, 48
Lee, G. H., Hwang, H. S., Sohn, J., & Lee, M. G. 2017, ApJ, 835, 280
Lieu, M., Smith, G. P., Giles, P. A., et al. 2016, A&A, 592, A4
Lomb, N. R. 1976, Ap&SS, 39, 447
López-Navas, E., Arévalo, P., Bernal, S., et al. 2023, MNRAS, 518, 1531
Maksym, W. P., Ulmer, M. P., & Eracleous, M. 2010, ApJ, 722, 1035
Maksym, W. P., Ulmer, M. P., Eracleous, M. C., Guennou, L., & Ho, L. C. 2013, MNRAS, 435, 1904
Maksym, W. P., Ulmer, M. P., Roth, K. C., et al. 2014, MNRAS, 444, 866
Maraston, C., Strömbäck, G., Thomas, D., Wake, D. A., & Nichol, R. C. 2009, MNRAS, 394, L107
Márquez, I., Masegosa, J., González-Martin, O., et al. 2017, Front. Astron. Space Sci., 4, 34
Masci, F. J., Laher, R. R., Rusholme, B., et al. 2019, PASP, 131, 018003
Maurogordato, S., Cappi, A., Ferrari, C., et al. 2008, A&A, 481, 593
Mislis, D., Schmitt, J. H. M. M., Carone, L., Guenther, E. W., & Pätzold, M. 2010, A&A, 522, A86
Moreno, J., Vogeley, M. S., Richards, G. T., & Yu, W. 2019, PASP, 131, 063001
Mushotzky, R. F., Edelson, R., Baumgartner, W., & Gandhi, P. 2011, ApJ, 743, L12
Nandra, K., George, I. M., Mushotzky, R. F., Turner, T. J., & Yaqoob, T. 1997, ApJ, 476, 70
Oh, S., Colless, M., D'Eugenio, F., et al. 2022, MNRAS, 512, 1765
Padovani, P., Alexander, D. M., Assef, R. J., et al. 2017, A&ARv, 25, 2
Pfeifle, R. W., Satyapal, S., Secrest, N. J., et al. 2019, ApJ, 875, 117
Pont, F., Zucker, S., & Queloz, D. 2006, MNRAS, 373, 231
Ponti, G., Papadakis, I., Bianchi, S., et al. 2012, A&A, 542, A83
Poulain, M., Paolillo, M., De Cicco, D., et al. 2020, A&A, 634, A50
Richardson, C. T., Allen, J. T., Baldwin, J. A., Hewett, P. C., & Ferland, G. J. 2014, MNRAS, 437, 2376
Rybicki, G. B., & Lightman, A. P. 1979, Radiative Processes in Astrophysics (Wiley-VCH)
Savitzky, A., & Golay, M. J. E. 1964, Anal. Chem., 36, 1627
Scargle, J. D. 1982, ApJ, 263, 835
Schmitt, A., Arnouts, S., Borges, R., et al. 2019, ASP Conf. Ser., 521, 398
Schreiber, C., Glazebrook, K., Nanayakkara, T., et al. 2018, A&A, 618, A85
Secrest, N. J., Ellison, S. L., Satyapal, S., & Blecha, L. 2020, MNRAS, 499, 2380
Serna, A., & Gerbal, D. 1996, A&A, 309, 65
Smith, K. L., Tandon, C. R., & Wagoner, R. V. 2021, ApJ, 906, 92
Taaki, J. S., Kamalabadi, F., & Kemball, A. J. 2020, AJ, 159, 283
Tamuz, O., Mazeh, T., & Zucker, S. 2005, MNRAS, 356, 1466
Tremaine, S., Gebhardt, K., Bender, R., et al. 2002, ApJ, 574, 740
Trevese, D., Boutsia, K., Vagnetti, F., Cappellaro, E., & Puccetti, S. 2008, A&A, 488, 73
Uttley, P., Edelson, R., McHardy, I. M., Peterson, B. M., & Markowitz, A. 2003, ApJ, 584, L53
van Roestel, J., Duev, D. A., Mahabal, A. A., et al. 2021, AJ, 161, 267
VanderPlas, J. T. 2018, ApJS, 236, 16
Vasylenko, A., Fedorova, E., & Zhdanov, V. 2015, BTSNU, 52, 39V
Vaughan, S. 2005, A&A, 431, 391
Vaughan, S., Edelson, R., Warwick, R. S., & Uttley, P. 2003, MNRAS, 345, 1271
Vaughan, S., Uttley, P., Markowitz, A. G., et al. 2016, MNRAS, 461, 3145
Virtanen, P., Gommers, R., Oliphant, T. E., et al. 2020, Nat. Methods, 17, 261
Wang, Z. F., Burke, C. J., Liu, X., & Shen, Y. 2023, MNRAS, 521, 99
Webb, N. A., Coriat, M., Traulsen, I., et al. 2020, A&A, 641, A136
Wise, J. H., Regan, J. A., O'Shea, B. W., et al. 2019, Nature, 566, 85
Young, M., Brandt, W. N., Xue, Y. Q., et al. 2012, ApJ, 748, 124
Yuk, H., Dai, X., Jayasinghe, T., et al. 2022, ApJ, 930, 110
Zhang, T., Ramakrishnan, R., & Livny, M. 1996, SIGMOD Rec., 25, 103
Zhou, X.-L., Zhang, S.-N., Wang, D.-X., & Zhu, L. 2010, ApJ, 710, 16
Zhu, S. F., & Xue, Y. Q. 2016, ApJ, 825, 56
Zu, Y., Kochanek, C. S., Kozłowski, S., & Udalski, A. 2013, ApJ, 765, 106

Appendix A: CGCG 077-102 NED01 light curves and CGCG 077-102 NED02 light curve after noise correction (*r*-band)

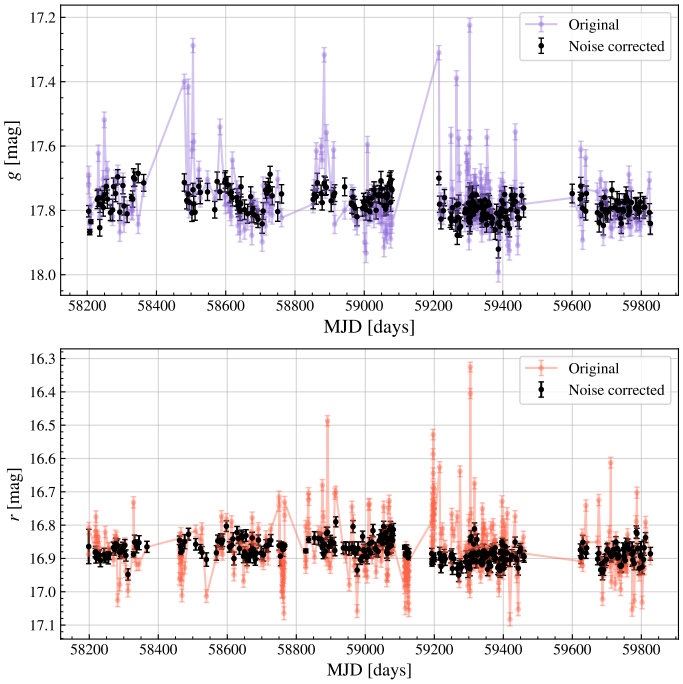

Fig. A.1. Light curves in g (top panel) and r (bottom panel) bands of NED01 before and after the noise correction with PDT and calculation of the intranight observation mean. The purple and orange connected dots represent the original light curves in their respective filters (g and r), and the black dots with error bars represent the noise-corrected light curve. We note that the light curve in r band becomes nearly flat after the noise correction, as we expected. However, the light curve in g band shows some periodic-like oscillations that are likely artifacts introduced by the PDT during the detrending process.

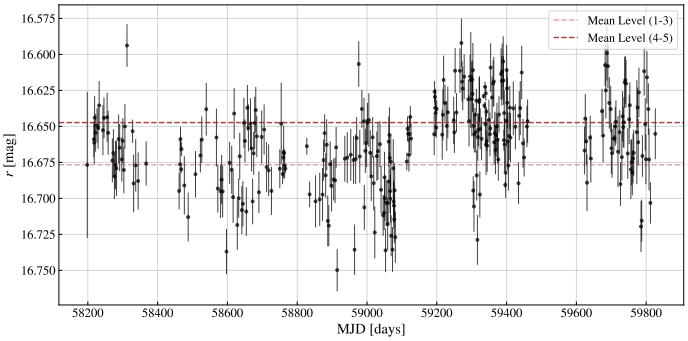

Fig. A.2. Light curve of NED02 in r-band (black dots). The dashed lines are the mean levels of the first three (light red) and the last two (dark red) cycles. In this case, we observe low-level variability after the noise correction. For this reason, we cannot confirm without any biases whether the light curve presents periodic-like oscillations or artifacts introduced during the detrending process. Furthermore, as discussed in Subsection 5.3.2, we cannot exclude the possibility of over-subtraction of the signal amplitude, which would prevent us from analyzing the light curve correctly in this filter.

In the framework of section 5, Fig. A.1 presents a comparison between the light curves in g and r bands of NED01 before and after the noise correction. Figure A.2 gives the light curve of NED02 galaxy in r-band after noise correction.

Appendix B: Lomb-Scargle periodogram

The Lomb-Scargle periodogram (LSP) is a method for periodicity analysis in time-series data (Lomb 1976; Scargle 1982). It is more widely used than classical techniques (such as the traditional Fourier methods) in astronomy due to its well-known efficiency in modeling time series with irregularly spaced data and gaps. The LSP is based on the least-squares fit of a sinusoidal model to the data at each frequency, but extensions of the standard LSP (as models that allow multiple Fourier terms and offsets) can also be found in the literature (see VanderPlas 2018, for more details).

We employed the `astropy.timeseries`[14] (Astropy Collaboration 2013, 2018, 2022) Python package to implement the LSP method for detecting periodic signals in the light curve. First, we applied a frequency cutoff in the periodogram for the low and high frequencies to avoid the effects of data gaps and white noise that can give us a false estimate of the period. At low frequencies, we cut the frequencies that correspond to periods longer than the interval between the first and last observation of the sample. For the high frequencies, we cut frequencies higher than the mean cadence of the data interval. Here, we took advantage of the LSP multiterm extension in order to obtain a more flexible model to describe the observed light curve accurately.

The LSP algorithm was not able to model the entire light curve correctly, likely because of the large data gaps between the last cycles of observations and the different mean levels in two distinct intervals of the light curve, as reported in Subsection 5.3.2 (see also Figure B.1). For this reason, we applied the LSP algorithm for the first three cycles of observations, excluding the last two from the analysis. Furthermore, we were not able to analyze the last two cycles separately because the algorithm fails to model this interval due to the gaps and the low number of observations.

Although we expected a noisier periodogram due to the multiterm Fourier model, which makes the detection of the correct peak difficult, the computed periodogram for a model with two Fourier terms shows an additional noise that increases toward low frequencies, similar to the shape of a power spectrum density (PSD) dominated by a red/pink noise (PSD $\propto f^{-\alpha}$). For this reason, we fitted a broken power law[15] on the PSD to estimate the red/pink noise continuum (see more details about "colored" noise PSDs in Vaughan (2005), Zhu & Xue (2016), Guo et al. (2017), for example), and we computed its confidence intervals with the bootstrap method. Here, we consider the highest peak above the 95% upper limit of the confidence interval to be the most probably correct peak. For a detailed discussion about why measuring the period uncertainties in terms of error bars is not recommended, see VanderPlas (2018).

The best-fitted Lomb-Scargle (LS) model with two Fourier terms on the first three cycles of observations, the power spectrum density, and the phase-folded light curve are shown in Figure B.1. Doubtless, the LS model is not flexible enough to describe the entire NED02 light curve, which requires a more

[14] https://docs.astropy.org/en/stable/timeseries/lombscargle.html
[15] https://docs.astropy.org/en/stable/api/astropy.modeling.powerlaws.BrokenPowerLaw1D.html

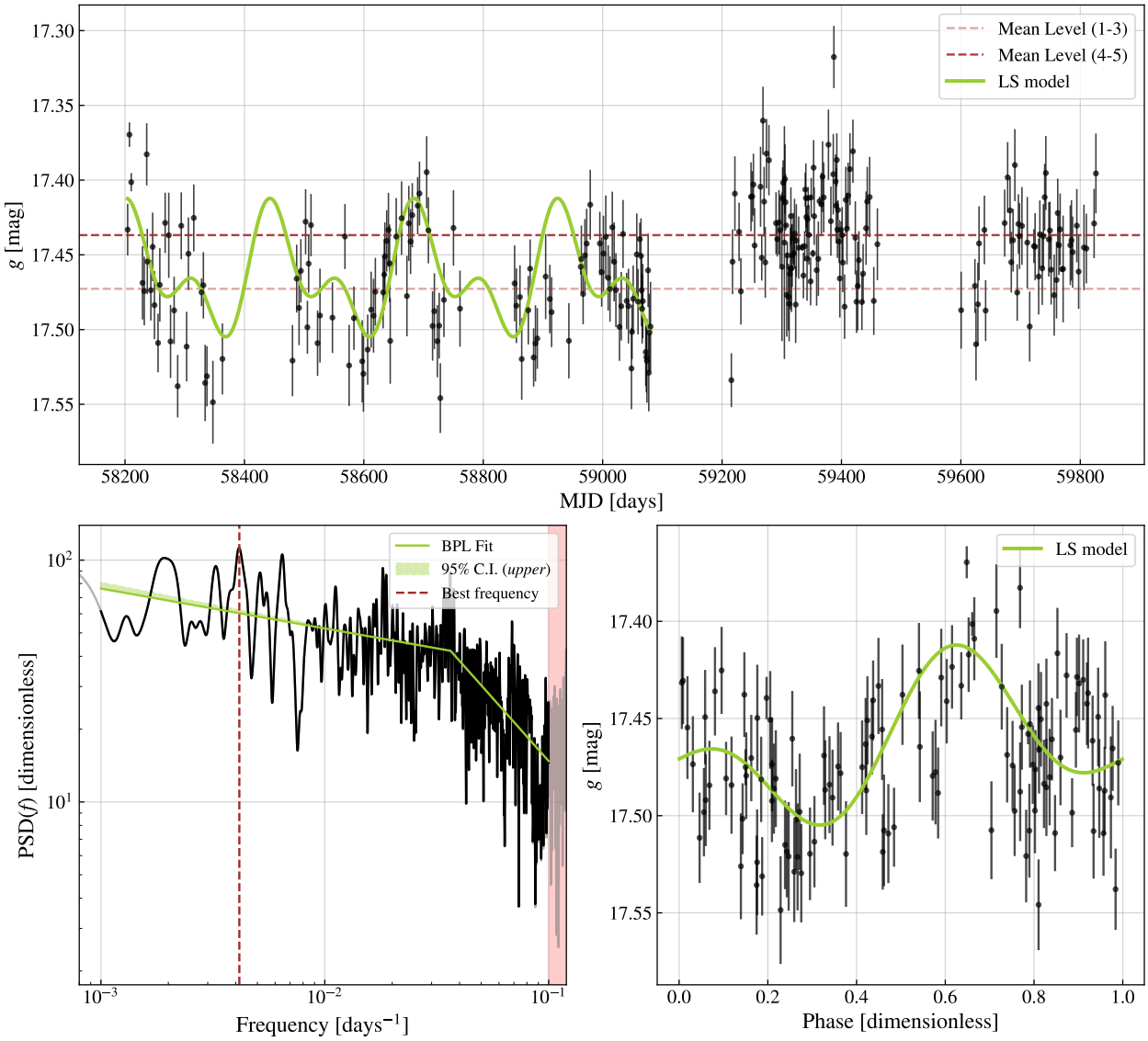

Fig. B.1. LSP analysis. *Top*: Detrended light curve of NED02 galaxy in g-band (black dots). The green line represents the best-fitted LS model with two Fourier terms on the first three cycles of observations. The dashed lines are the mean levels of the first three (light red) and the last two (dark red) cycles. *Bottom left*: LSP. The solid black line represents the PSD, the light green line is the BPL best fit (a break frequency of $f_{break} = 0.036 \pm 0.001$ days^{-1}, low-frequency slope of $\alpha_1 = 0.164 \pm 0.007$, and high-frequency slope of $\alpha_2 = 1.04 \pm 0.03$), the light shaded green region is the 95% upper limit of the C.I., and the light-red shaded region shows the frequency cutoff (< 0.001 days^{-1} and > 0.1 days^{-1}). The vertical dark red dashed line shows the highest peak above the 95% upper limit, corresponding to a frequency of ~ 0.004 days^{-1}. The PSD is dimensionless because the uncertainties were specified within the `LombScargle`/astropy implementation. *Bottom right*: Phase-folded light curve (black dots) for the first three cycles of observations, with the best-fit LS model (solid green line). The folding period is 240.9 days.

complex model to fulfill this task, such as stochastic models. Also, it is well known that red noise signal can be confused with true periodic oscillations, leading us to detect false periodicities in AGNs (e.g., Vaughan et al. 2016). Therefore, this method cannot confirm the presence of a real periodic signal in the NED02 light curve.